



HAL
open science

Modeling of diffuse auroral emission at Mars: Contribution of MeV protons

Yuki Nakamura, Naoki Terada, François Leblanc, Ali Rahmati, Hiromu Nakagawa, Shotaro Sakai, Sayano Hiruba, Ryuho Kataoka, Kiyoka Murase

► To cite this version:

Yuki Nakamura, Naoki Terada, François Leblanc, Ali Rahmati, Hiromu Nakagawa, et al.. Modeling of diffuse auroral emission at Mars: Contribution of MeV protons. *Journal of Geophysical Research Space Physics*, 2022, 127 (1), pp.e2021JA029914. 10.1029/2021JA029914 . insu-03517910

HAL Id: insu-03517910

<https://insu.hal.science/insu-03517910>

Submitted on 10 Jan 2022

HAL is a multi-disciplinary open access archive for the deposit and dissemination of scientific research documents, whether they are published or not. The documents may come from teaching and research institutions in France or abroad, or from public or private research centers.

L'archive ouverte pluridisciplinaire **HAL**, est destinée au dépôt et à la diffusion de documents scientifiques de niveau recherche, publiés ou non, émanant des établissements d'enseignement et de recherche français ou étrangers, des laboratoires publics ou privés.

1 **Modeling of diffuse auroral emission at Mars: Contribution of MeV protons**

2
3 Yuki Nakamura^{1,2}, Naoki Terada¹, Francois Leblanc², Ali Rahmati³, Hiromu Nakagawa¹,
4 Shotaro Sakai^{1,4}, Sayano Hiruba¹, Ryuho Kataoka^{5,6}, and Kiyoka Murase^{5,6}

5
6 ¹Graduate School of Science, Tohoku University, Sendai, Japan

7 ²LATMOS/CNRS, Sorbonne Université, Paris, France

8 ³Space Sciences Laboratory, University of California, Berkeley, CA, USA

9 ⁴Planetary Plasma and Atmospheric Research Center, Graduate School of Science,
10 Tohoku University, Sendai, Japan

11 ⁵National Institute of Polar Research, Tokyo, Japan

12 ⁶The Graduate University for Advanced Studies, SOKENDAI, Kanagawa, Japan

13
14 Corresponding author: Yuki Nakamura (yuki.nakamura.r2@dc.tohoku.ac.jp)

15
16
17 **Key Points:**

- 18
- 19 • A Monte Carlo model was developed to investigate the contributions of
precipitating electrons and protons to the diffuse auroral emission.
 - 20 • Proton-induced CO₂⁺ UVD emissions have lower peak altitudes than electron-
21 induced emissions.
 - 22 • The MAVEN/IUVS limb emission profiles of CO₂⁺ UVD during two SEP
23 events were reproduced by considering the contribution of SEP protons.
- 24

25

26 **Abstract (236 words/ up to 250 words)**

27 The Solar Energetic Particle and Imaging UltraViolet Spectrograph (IUVS) instruments
28 onboard the Mars Atmosphere and Volatile EvolutionN (MAVEN) spacecraft discovered
29 diffuse aurora that span across the nightside of Mars due to the interaction of solar
30 energetic particles (SEPs) with the Martian atmosphere. However, it is unclear whether
31 the diffuse aurora originates from energetic electrons or protons. We have developed a
32 Monte Carlo model to calculate the limb intensity profile of the CO₂⁺ ultraviolet doublet
33 (UVD) due to precipitation of energetic electrons and protons with energy ranges from
34 100 eV to 100 keV and from 50 keV to 5 MeV, respectively. We used electron and proton
35 fluxes observed by MAVEN during the December 2014 SEP event and the September
36 2017 SEP event. Our results showed that proton-induced CO₂⁺ UVD emission has a lower
37 peak altitude than electron-induced CO₂⁺ UVD emission. The calculated peak altitudes
38 of the CO₂⁺ UVD limb profiles are 76 km and 68 km in the December 2014 event and the
39 September 2017 event, respectively. Extending the energy to 500 keV for electrons and
40 20 MeV for protons further improved our comparison to the IUVS observations. We have
41 succeeded in reproducing peak altitudes and shapes of the observed CO₂⁺ UVD limb
42 profiles using the SEP flux observed by MAVEN. This was possible by taking into
43 account the contribution of energetic protons, indicating that both energetic electrons and
44 protons contribute to producing the observed diffuse aurora.

45

46

47 **1. Introduction**

48 Solar energetic particles (SEPs) can easily penetrate deep into the atmosphere owing to
49 insufficient magnetospheric and atmospheric shielding of Mars (Leblanc et al., 2002).
50 Penetration of SEPs into the Martian atmosphere leads to increased ionization, heating of
51 the atmosphere and alteration of the atmospheric chemistry (Leblanc et al., 2002; Jolitz
52 et al. 2017; Haider and Masoom, 2019; Gérard et al., 2017; Lingam et al., 2018). One of
53 the consequences of the interaction of SEPs with the Martian atmosphere is the
54 production of auroral emissions (Schneider et al., 2015).

55

56 There are three types of aurora that have been identified on Mars: discrete aurora, proton
57 aurora, and diffuse aurora. The discrete aurora was first detected by the Mars Express in
58 the crustal magnetic field region (Bertaux et al., 2005) and is believed to be caused by the
59 acceleration of electrons due to the electric potential along open magnetic field lines
60 (Brain et al., 2006). The discrete aurora is characterized by a strongly localized patch-like

61 morphology of the emissions and a peak altitude of approximately 120 km, which
62 indicates that precipitation of a few keV electrons causes the discrete aurora (e.g., Bertaux
63 et al., 2005). The proton aurora was first detected by the Mars Atmosphere and Volatile
64 EvolutionN (MAVEN) spacecraft on the dayside of Mars (Deighan et al., 2018; Ritter et
65 al., 2018). Proton aurorae are produced by solar wind protons that are neutralized by
66 charge exchange with exospheric hydrogen atoms outside the Mars' induced
67 magnetosphere. They travel without losing energy up to the atmosphere, where they
68 collide with Mars' main atmospheric constituent, CO₂, become excited and produce
69 Lyman- α emissions. These proton aurorae are visible preferentially during the dayside
70 southern summer solstice (near the solar longitude (Ls), which is 270° when the Mars
71 hydrogen exosphere is the densest) and display a brightness profile peaking at an altitude
72 of approximately 120 km (Hughes et al., 2019).

73

74 Recently, MAVEN discovered a new type of aurora, namely, diffuse aurora, that spans
75 the Mars nightside and results from the interaction of SEPs with the Martian atmosphere
76 (Schneider et al., 2015, 2018). This new type of diffuse aurora on Mars is characterized
77 by global brightening and by its low peak altitude of ~60 km, which indicates that more
78 energy is deposited deep in the Martian atmosphere than previously observed. Previous
79 models suggested that 100 keV of monoenergetic electron precipitation should have been
80 at the origin of the low altitude (~60 km) peak of the limb emission; however, no model
81 was able to reproduce the observed emission profiles by using the observed energetic
82 electron flux (Schneider et al., 2015; Gérard et al., 2017; Haider and Masoom, 2019).
83 Previous auroral emission models did not take into account the contribution of MeV
84 proton precipitation, although MeV protons can penetrate down to ~70 km altitude as
85 well (Jolitz et al., 2017). Observations of SEP electron and ion fluxes with the Solar
86 Energetic Particle instrument during the aurorae observed by Imaging UltraViolet
87 Spectrograph (IUVS) instruments onboard MAVEN suggested that both electron and
88 proton energetic populations could have been at the origin of the diffuse aurora (Schneider
89 et al., 2018).

90

91 We have developed a Monte Carlo model of Particle TRansport In Planetary atmospheres
92 (PTRIP). PTRIP describes the motion of electrons, protons and hydrogen atoms in the
93 Martian atmosphere. We calculated the limb intensity profile of the CO₂⁺ ultraviolet
94 doublet (UVD) due to precipitating electrons and protons with energies ranging from 100
95 eV - 100 keV and 50 keV - 5 MeV, respectively, as observed by MAVEN during the
96 December 2014 SEP event and September 2017 SEP event.

97

98

99 **2. Model Description**

100 PTRIP is a Monte Carlo model that is designed to examine the transport and collisions of
101 electrons, protons and hydrogen atoms that precipitate into the Martian atmosphere. The
102 key assumptions in this study are as follows: (1) we ignore the effects of the electric and
103 magnetic fields on the particle trajectory, (2) atmospheric particles are at rest with respect
104 to incident particles, (3) each incident particle is independent and does not collide or
105 interact with other incident particles, and (4) initial incident angles with respect to the
106 atmosphere are isotropically distributed over one hemisphere directed vertically
107 downward. PTRIP solves the three velocity components of the particle but takes into
108 account only the trajectory of the particle along the altitude. Incident particles are traced
109 below an altitude of 500 km. This study focuses on the emission rate of CO_2^+ UVD with
110 an ionizing threshold energy of ~ 18 eV, so particles below 15 eV are suppressed from the
111 simulation.

112

113 **2.1 Monte Carlo Transport Model**

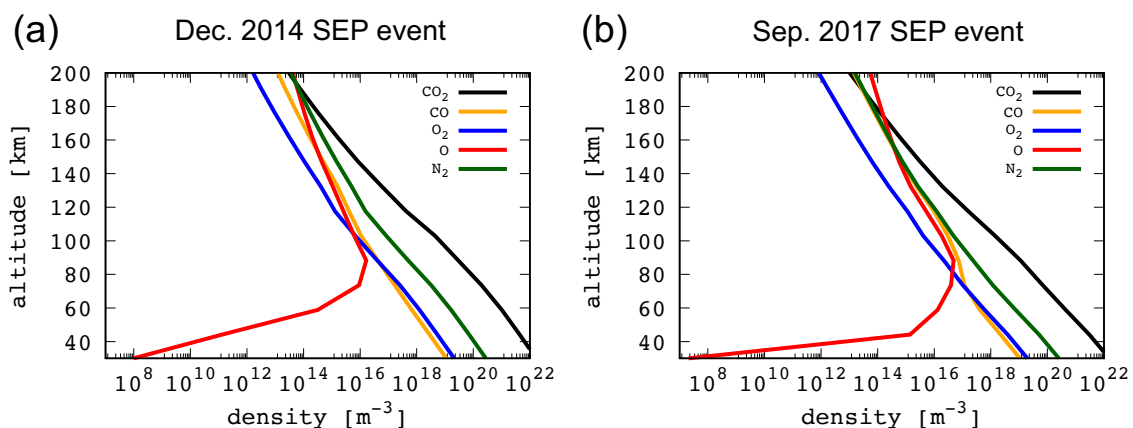
114 In PTRIP, a random number is used to determine whether there is a collision at each time
115 step for each incident particle. The collision probability P_c for a particle traveling along
116 a distance Δl is expressed as:

$$117 \quad P_c = 1 - \exp \left[- \sum_s n_s(\mathbf{l}) \sigma_s^T(E) \Delta l \right] \quad (1)$$

118 where $n_s(\mathbf{l})$ is the number density of the s th atmospheric species at particle location \mathbf{l} ,
119 $\sigma_s^T(E)$ is the total collisional cross section of the s th atmospheric species for particle
120 energy E , and $\Delta l = |v\Delta t|$, where v is the absolute velocity of the particle and Δt is
121 the time step. A collision occurs if a random number determined from a uniform
122 distribution in a range $[0, 1]$ is less than P_c . Since P_c is the sum of the probabilities for
123 n collisions during Δt ($n = 1, 2, 3, \dots$), the accuracy of the collision probability
124 depends on Δt . Δt is determined so that the number of collisions not taken into account
125 during Δt is less than 0.01, which requires P_c to be less than 0.1 (Vahedi and Surrendra,
126 1995). If a collision occurs, another random number is used to determine the type of
127 collision so that the probability of each type of collision is weighted by the ratio of the
128 frequency of each type of collision to the total collision frequency (Vahedi and Surrendra,
129 1995).

130

131 Several inputs are required by PTRIP. Regarding the incident particles, we need to define
 132 the initial type (electron or proton), the initial energy and the number of incident particles.
 133 The initial energy of electrons is a set of 16 logarithmically spaced energy bins in a range
 134 [100 eV - 100 keV], and the initial energy of protons is a set of 11 logarithmically spaced
 135 energy bins in a range [50 keV - 5 MeV]. The number of incident particles at each incident
 136 energy is selected to be 1000. Regarding the atmospheric species and their interactions
 137 with the incident particles, we defined the atmospheric neutral density profiles, the
 138 inelastic and elastic cross sections, energy loss, scattering angle distributions, and the
 139 produced secondary electron energy. In this study, we use the atmospheric density profiles
 140 for the 5 main species (CO₂, CO, N₂, O₂ and O) from the nightside of the northern
 141 hemisphere as calculated by the Mars Climate Database (MCD) version 5.3 (Millour et
 142 al., 2018). CO₂ is the most important constituent in this study because we focus on the
 143 ionization of CO₂ to generate CO₂⁺ UVD emissions. Figure 1 shows atmospheric neutral
 144 density profiles used in this study for the December 2014 SEP event and September 2017
 145 SEP event. The solar longitude (Ls) was 255° (near perihelion) on 20 December 2014 and
 146 60° (near aphelion) on 13 September 2017, corresponding to the season of atmospheric
 147 inflation and contraction on Mars, respectively (e.g., Forget et al., 2009). The solar
 148 activity and the dust load are set to be average. The latitude and local time are set to be
 149 35°N, 00:00, respectively, to match the IUVS observation geometry when the diffuse
 150 aurora profile was obtained (Schneider et al., 2015). The CO₂ number density at an
 151 altitude of 80 km was $8.5 \times 10^{19} \text{ m}^{-3}$ on 20 December 2014 and $3.1 \times 10^{19} \text{ m}^{-3}$ on 13
 152 September 2017. Other inputs regarding the interactions of incident particles with
 153 atmospheric species are explained in the following sections.
 154



155
 156 Figure 1(a) Atmospheric density profile on 20 December 2014 and (b)
 157 atmospheric density profile on 13 September 2017 used in the Monte
 158 Carlo simulations. These density profiles were calculated by the Mars

2.2 Collisional Cross Sections

PTRIP takes into account elastic and inelastic cross sections of impacting electrons, protons and hydrogen atoms with atmospheric species. First, we describe the elastic and inelastic cross sections due to electron impacts. We calculate the total elastic cross sections of CO₂, CO, N₂, O₂ and O by the formula of Yalcin et al. (2006), which is applicable to 1 keV - 1 MeV. Below 1 keV, we use the total elastic cross section of CO₂ recommended by Itikawa (2002), of CO recommended by Itikawa (2015), of N₂ recommended by Itikawa (2006), of O₂ recommended by Itikawa (2009) and of O in Porter et al. (1978, 1987). The analytic fits of differential ionization cross sections of CO₂ are taken from Bhardwaj and Jain (2009), including the production of 4 excited states (X²Π_g, A²Π_u, B²Σ_u⁺, and C²Σ_g⁺), dissociative ionization, and double ionization. The analytic fits of the differential ionization cross sections of N₂, O₂ and O are taken from Jackman et al. (1977). The accuracy of the energetic electron transport model depends on the accuracy of the ionization cross section of CO₂ because energetic electrons lose energy mostly by ionizing collisions with CO₂. The total ionization cross section of CO₂ used in this study was $\sim 3.0 \times 10^{-22} \text{ m}^2$ at 100 keV, which agrees well with the observed value of $\sim 3.2 \times 10^{-22} \text{ m}^2$ at 100 keV by Rieke and Prepejchal (1972). The analytic fits of differential excitation cross sections of CO₂ are taken from Bhardwaj and Jain (2009). For the fundamental three vibrational excitations of CO₂, (010), (100), and (001), within the energy range of 1.5 eV to 30 eV are taken from Itikawa (2002).

Second, we describe the elastic and inelastic cross sections due to proton impacts. The differential screened Rutherford cross section for the elastic scattering of protons by atoms without correction for relativistic effects can be expressed as:

$$\frac{d\sigma}{d\Omega}(E, \theta) = \left(\frac{Ze}{8\pi\epsilon_0 E} \right)^2 \frac{1}{(1 - \cos\theta + 2\eta)^2} \quad (2)$$

where Ω is the solid angle, Z is the atomic number of the target particle, e is the elementary charge, ϵ_0 is the permittivity in space, E is the incident proton energy in units of eV, θ is the scattering angle, and η is the screening parameter. The screening parameter η is expressed as (Nigam et al., 1959):

$$\eta = \frac{1}{4} \left(1.12 \frac{\lambda}{2\pi a} \right)^2 \quad (3)$$

where λ is the de Broglie wavelength ($\lambda = h/p$, h is the Planck constant and p is momentum of a proton) and a is the Fermi radius of the atom ($a = 0.885a_0Z^{-1/3}$, a_0

193 is the Bohr radius $a_0 = 5.29 \times 10^{-11}$ [m]). The total elastic cross section can be expressed
 194 by integrating equation (2) over the solid angle Ω :

$$195 \quad \sigma(E) = \left(\frac{Ze}{8\pi\epsilon_0 E} \right)^2 \frac{\pi}{\eta(1+\eta)} \quad (4)$$

196 For the study of proton transport in a planetary atmosphere, the differential and total
 197 elastic cross sections from Kallio and Barabash (2001) have been widely used in many
 198 models (e.g., Fang et al., 2013; Jolitz et al., 2017) and are based on the observation of
 199 hydrogen atom-impact elastic cross sections up to 5 keV (Newman et al., 1986; Noël and
 200 Prölss, 1993). The observed differential elastic cross section of 5.34 MeV proton impacts
 201 on carbon atoms at a scattering angle of 60 degrees is 3.2×10^{-30} m² (Shute et al., 1962);
 202 however, the differential elastic cross section from Kallio and Barabash (2001) for
 203 incident 5.34 MeV proton at a scattering angle of 60 degrees is 8.2×10^{-27} m², which is
 204 calculated by the formula described in Kallio and Barabash (2001); this value is 3 orders
 205 of magnitude larger than the observed value reported by Shute et al. (1962). The
 206 differential elastic cross section of carbon for an incident 5.34 MeV proton at the
 207 scattering angle of 60 degrees calculated by equation (2) is 2.6×10^{-30} m², which is in good
 208 agreement with the observed differential elastic cross section from Shute et al. (1962).

209
 210 The analytic fit of the differential ionization cross section of CO₂ due to proton impacts
 211 are taken from Rudd et al. (1983), including the production of 4 excited states ($X^2\Pi_g$,
 212 $A^2\Pi_u$, $B^2\Sigma_u^+$, and $C^2\Sigma_g^+$). The analytic fits of differential ionization cross sections of CO,
 213 N₂ and O₂ are also taken from Rudd et al. (1983). The total ionization cross section of O
 214 is taken from Basu et al. (1987) for above 2 keV and from Haider et al. (2002) for below
 215 2 keV. The analytic fits of differential charge exchange cross sections of CO₂ above 10
 216 keV are taken from Rudd et al. (1983), including the production of 4 excited states ($X^2\Pi_g$,
 217 $A^2\Pi_u$, $B^2\Sigma_u^+$, and $C^2\Sigma_g^+$). The total charge exchange cross section of CO₂ below 10 keV
 218 is taken from Haider et al. (2002), and the branching ratio is assumed to be the one for a
 219 10 keV proton in Rudd et al. (1983). The analytic fits of differential charge exchange
 220 cross sections of CO, N₂ and O₂ are taken from Rudd et al. (1983). The total charge
 221 exchange cross section of O is taken from Basu et al. (1987) for above 1 keV and Haider
 222 et al. (2002) for below 1 keV.

223
 224 Finally, we describe the elastic and inelastic cross sections due to hydrogen atom impacts.
 225 The total elastic cross sections are calculated by the formula of Noël and Prölss (1993),
 226 and the parameters for this formula are taken from Kallio and Barabash (2001). Since
 227 there is almost no information on the hydrogen atom-impact inelastic cross sections of

228 CO₂, we approximated these cross sections. The total ionization and electron stripping
229 cross sections of CO₂ are assumed to be identical to the hydrogen atom impact total
230 ionization and electron stripping cross section of O₂, as in many previous studies (e.g.,
231 Kallio and Barabash, 2001; Jolitz et al., 2017). The total ionization and electron stripping
232 cross sections of O₂ are taken from Basu et al. (1987) for above 1 keV and from Haider
233 et al. (2002) for below 1 keV. The branching ratio of CO₂⁺ (B²Σ_u⁺) to total CO₂ ionization
234 is assumed to be 0.1, which is identical to the branching ratio due to proton impacts (Rudd
235 et al., 1983). The total ionization and electron stripping cross sections of CO are also
236 assumed to be identical to those of O₂. The total ionization and electron stripping cross
237 sections of N₂ are taken from Kozelov et al. (1992). The total ionization cross section of
238 O is taken from Basu et al. (1987) for above 2 keV and Haider et al. (2002) for below 2
239 keV, and the electron stripping cross section of O is taken from Basu et al. (1987) for
240 above 10 keV and from Haider et al. (2002) for below 10 keV. The cross section of CO₂
241 with hydrogen atoms leading to Lyman-α emission is taken from Haider et al. (2002).

242

243 **2.3 Energy Loss, Scattering Angle, and Secondary Electron Energy**

244 If a collision occurs, the energy loss, scattering angle and secondary electron energy are
245 calculated for each type of collision. If a collision is elastic, the scattering angle and
246 energy loss are calculated. The scattering angle distribution of electrons is taken from
247 Porter et al. (1987) at low energy (CO₂: below 500 eV, CO: below 800 eV, O₂: below 500
248 eV, N₂: below 1 keV, and O: below 1 keV) and calculated by the formula of Yalcin et al.
249 (2006) above these energies. The scattering angle of electrons is calculated randomly by
250 using these scattering angle distributions (e.g., Solomon, 2001). The scattering angle of
251 protons can be randomly calculated by using the differential elastic cross section in
252 equation (2). The scattering angle distribution of hydrogen atoms is calculated by the
253 formula of Noël and Prölss (1993), and the parameters for this formula are taken from
254 Kallio and Barabash (2001). The scattering angle of hydrogen atoms is calculated
255 randomly by using this scattering angle distribution (Noël and Prölss, 1993). Energy loss
256 in elastic collision is calculated by solving equations of energy and momentum
257 conservation in a binary collision.

258

259 If a collision is inelastic, incident particles lose a fixed amount of energy equal to the
260 energy threshold for ionization, excitation, charge exchange, electron stripping and
261 Lyman-α. Threshold energies are taken from the references of cross sections as already
262 explained in the previous section. In all inelastic collisions, the scattering angle is
263 assumed to be 0 with the assumption of strong forward-peaked scattering (Solomon,

2001). If a collision leads to ionization, the incident particle also loses the amount of energy associated with the produced secondary electron. Secondary electron energy due to an electron impact is randomly calculated by the formula of Green and Sawada (1972) and Jackman et al. (1977). The secondary electron energy due to a proton impact is randomly calculated by the formula of Solomon (2001). The secondary electron energy due to a hydrogen impact is also calculated by this method. If a collision leads to electron stripping from a hydrogen atom, the calculated secondary electron energy is in the rest frame of the hydrogen atom, which is then converted to the energy in the rest frame of the atmosphere. All the produced secondary electrons are added to the simulation. Electrons lose energy to thermal electrons via Coulomb collisions. The energy transfer rate from incident electrons to thermal electrons is calculated by the formula of Swartz et al. (1971).

276

277 **2.4 Method for Converting Particle Trajectories into Flux**

278 The collision rate as a function of altitude z for the j th collision type (e.g. ionization rate) of the s th atmospheric species in an SEP event, $P_s^j(z)$, can be calculated by integrating the collision rate of the incident flux of $1 \text{ cm}^{-2} \text{ s}^{-1}$ for incident energy E_0 as a function of altitude $p_s^j(z, E_0)$ weighted by the energy flux spectrum $f(E_0) \text{ cm}^{-2} \text{ s}^{-1}$ observed by MAVEN:

$$283 \quad P_s^j(z) = \int f(E_0) p_s^j(z, E_0) dE_0 \quad (5)$$

284 In the Monte Carlo model, the collision rate $p_s^j(z, E_0)$ can be calculated by counting the number of collisions leading to ionization with atmospheric particles in a given cell; however, this counting method is noisy at high altitudes where the collision frequency is small, and minor types of collisions that do not occur frequently. We convert the trajectories of all the particles into a flux and mean pitch angle of the incident particles as a function of altitude and energy. The ionization rate can then be calculated by using the flux, mean pitch angle, neutral density and collisional cross section. The flux and mean pitch angle are determined at each altitude z ($0 \leq z \leq 500 \text{ km}$ with 1 km resolution) and energy grid E ($15 \leq E \leq E_0 \text{ eV}$, logarithmically spaced with 10 energy bins in one digit). The collision rate of the j th collision type of the s th atmospheric species within a cell of $[z, z + \Delta z] \times [E, E + \Delta E]$ of the incident energy E_0 with the incident flux at the top of the model of $1 \text{ cm}^{-2} \text{ s}^{-1}$, $p_s^j(z, E_0) \text{ cm}^{-3} \text{ s}^{-1}$, can be expressed by using the flux as:

$$296 \quad p_s^j(z, E_0) = n_s(z) \int_0^{E_0} \sigma_s^j(E) \left[\frac{\phi^+(z, E, E_0)}{\bar{\mu}^+(z, E, E_0)} + \frac{\phi^-(z, E, E_0)}{\bar{\mu}^-(z, E, E_0)} \right] dE \quad (6)$$

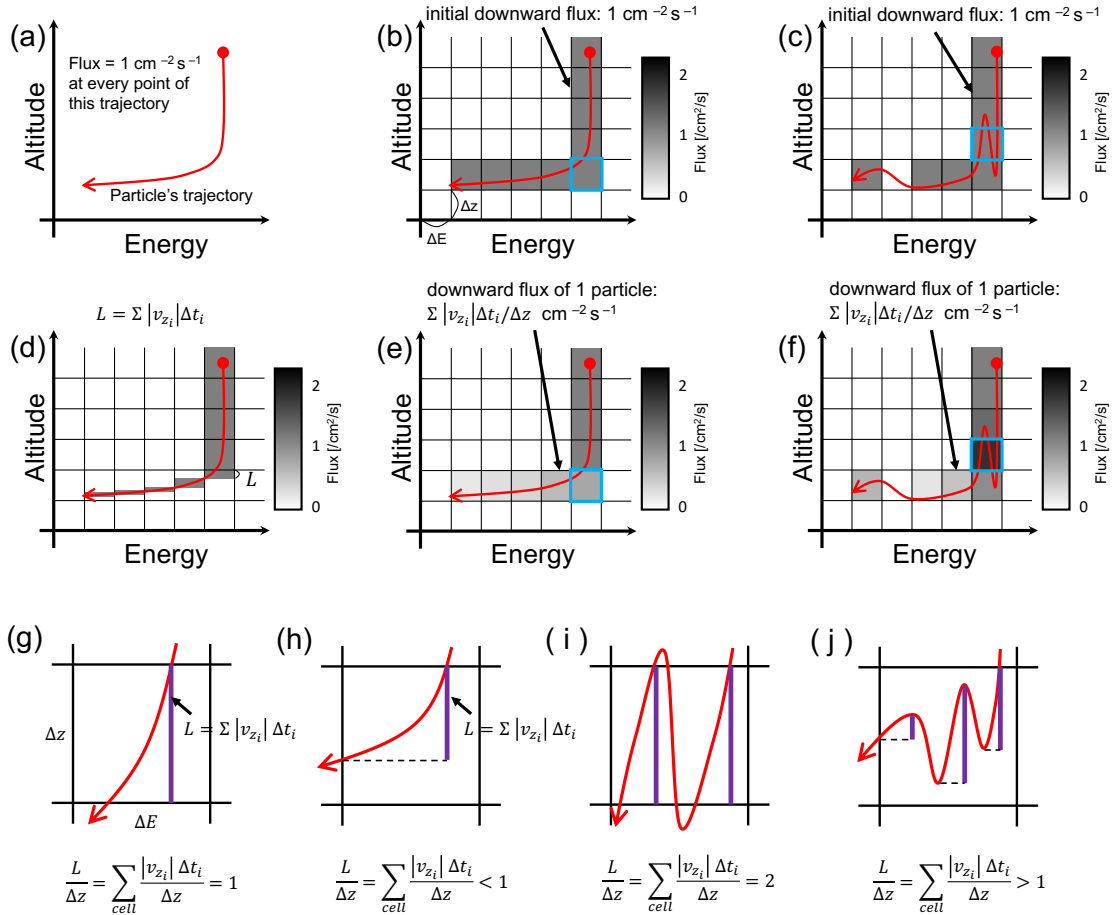
297 where $n_s(z)$ is the number density of the s th atmospheric species at the altitude grid of

298 z , $\sigma_s^j(E)$ is the cross section of the j th collision type of the s th atmospheric species at
 299 the energy grid of E , $\phi^+(z, E, E_0)$ and $\phi^-(z, E, E_0)$ are upward and downward fluxes
 300 with the incident flux of the incident energy E_0 at the top of the model of $1 \text{ cm}^{-2} \text{ s}^{-1}$
 301 within a cell of $[z, z + \Delta z] \times [E, E + \Delta E]$, respectively, and $\bar{\mu}^+(z, E, E_0)$ and $\bar{\mu}^-(z, E, E_0)$
 302 are the mean cosine pitch angles of upward and downward moving particles within a cell
 303 $[z, z + \Delta z] \times [E, E + \Delta E]$ for incident energy E_0 , respectively.

304

305 We constructed a method of converting all particle trajectories into fluxes in the following
 306 flow: (1) converting the trajectory of a single particle into a flux and (2) taking the average
 307 of all the fluxes converted from each particle's trajectory. In Figure 2a, the red line
 308 illustrates the trajectory of a single particle in the altitude-energy frame. To convert the
 309 trajectory into a flux, one particle is injected (red dot in Figure 2a) per second, and all the
 310 particles follow the same trajectory. The flux is always $1 \text{ cm}^{-2} \text{ s}^{-1}$ at every point of the
 311 trajectory. In Figure 2b, the initial downward flux at the cell $[z, z + \Delta z] \times [E, E + \Delta E]$ is 1
 312 $\text{cm}^{-2} \text{ s}^{-1}$ if a particle enters the cell $[z, z + \Delta z] \times [E, E + \Delta E]$ with negative vertical velocity,
 313 and vice versa. For better understanding, another example of a trajectory is shown in
 314 Figure 2c. The initial flux $1 \text{ cm}^{-2} \text{ s}^{-1}$ works well when a particle crosses the whole cell
 315 without being backscattered (an enlarged view of a cell in Figure 2g). The initial flux
 316 overestimates the flux if a particle does not cross the whole cell without being
 317 backscattered (e.g., a cell with a blue frame in Figure 2b and an enlarged view of a cell
 318 in Figure 2h), and underestimates the flux if it returns to the cell (e.g., a cell with a blue
 319 frame in Figure 2c and an enlarged view of a cell in Figure 2i) and if it is frequently
 320 backscattered within the cell (e.g., an enlarged view of a cell in Figure 2j), respectively.
 321 The overestimation and underestimation of the initial flux can be improved by
 322 multiplying the flux of $1 \text{ cm}^{-2} \text{ s}^{-1}$ by the ratio between the vertical length L traveled by
 323 the particle within the cell, and the vertical cell size Δz , $L/\Delta z$. The vertical length L
 324 within the cell can be calculated numerically by $L = \sum |v_{z_i}| \Delta t_i$ within the cell, where
 325 v_{z_i} is the vertical velocity of the i th particle and Δt_i is a time step size (Figure 2d). For
 326 example, for the downward flux, L is calculated numerically by summing $|v_{z_i}| \Delta t_i$ at
 327 each time step within the cell only if the particle moves downward ($v_{z_i} < 0$). If a particle
 328 crosses the whole cell and is not backscattered into this cell, the flux is kept at $1 \text{ cm}^{-2} \text{ s}^{-1}$
 329 (Figure 2g: L is the length of a vertical purple bar). If a particle does not cross the whole
 330 cell without being backscattered, the flux is then less than 1 (e.g., a cell with a blue frame
 331 in Figure 2e, and an enlarged view of a cell in Figure 2h: L is the length of a vertical
 332 purple bar). If a particle re-enters the cell or if it is frequently backscattered within the
 333 cell, the flux is then more than $1 \text{ cm}^{-2} \text{ s}^{-1}$ (e.g., a cell with a blue frame in Figure 2f, and

334 an enlarged view of a cell in Figure 2i and 2j: L is the sum of the length of vertical purple
 335 bars).
 336



337

338 Figure 2 Schematic illustration of the method of converting the trajectory
 339 of a single particle (red lines) into a flux (see text for details). (g-j) The
 340 vertical purple bars represent the vertical length that traveled by a
 341 downward moving particle within the cell.

342

343 Finally, this flux of a single incident particle is calculated for each of the N incident
 344 particles, and taking average of all the converted fluxes yields the expressions of the
 345 upward and downward fluxes at each cell, corresponding to the flux of $1 \text{ cm}^{-2} \text{ s}^{-1}$ at the
 346 top of the atmosphere (Figure 2e and 2f). The upward and downward fluxes for an initial
 347 energy E_0 with the model topside incident flux of $1 \text{ cm}^{-2} \text{ s}^{-1}$ ($\phi^+(z, E, E_0)$ and
 348 $\phi^-(z, E, E_0)$, respectively) are expressed as:

$$349 \quad \phi^+(z, E, E_0) = \frac{1}{N} \sum_{i=1}^N \sum_{\substack{z < z_i \leq z + \Delta z \\ E < E_i \leq E + \Delta E \\ v_{z_i} \geq 0}} \frac{|v_{z_i}| \Delta t_i}{\Delta z} \quad (7)$$

$$350 \quad \phi^-(z, E, E_0) = \frac{1}{N} \sum_{i=1}^N \sum_{\substack{z < z_i \leq z + \Delta z \\ E < E_i \leq E + \Delta E \\ v_{z_i} < 0}} \frac{|v_{z_i}| \Delta t_i}{\Delta z} \quad (8)$$

351 The upward and downward mean cosine pitch angles of the i th particle ($\bar{\mu}^+(z, E, E_0)$
 352 and $\bar{\mu}^-(z, E, E_0)$) at the cell $[z, z + \Delta z] \times [E, E + \Delta E]$ are calculated by averaging the
 353 upward and downward cosine pitch angles, respectively. Averaging $\bar{\mu}^+(z, E, E_0)$ and
 354 $\bar{\mu}^-(z, E, E_0)$ for all particles that enter the cell $[z, z + \Delta z] \times [E, E + \Delta E]$ gives the mean
 355 cosine pitch angles of upward and downward particles $\bar{\mu}^+(z, E, E_0)$ and $\bar{\mu}^-(z, E, E_0)$,
 356 respectively. Examples of the calculated upward and downward fluxes, the mean cosine
 357 pitch angles, and a comparison of the two methods of deriving the ionization rate,
 358 counting the number of ionization collisions and using the converted fluxes, are shown
 359 in Figure S1-S5 in the supplementary materials. The ionization rate calculated by the
 360 method using the converted fluxes is in very good agreement with the counting method.

361

362 **2.5 Limb Intensity of CO₂⁺ UVD**

363 The focus of this study is to derive the limb intensity profile of CO₂⁺ UVD emissions.
 364 CO₂⁺ UVD is emitted by the transition of CO₂⁺ from the B²Σ_u⁺ state to the ground state
 365 X²Π_g. The transition from CO₂⁺ (B²Σ_u⁺) has another branch of transition to the A²Π_u state.
 366 We considered the branching ratio of the reaction leading to CO₂⁺ UVD emission to be
 367 equal to 0.5 (Fox and Dalgano, 1979; Bhardwaj and Jain, 2013; Haider and Masoom,
 368 2019). The CO₂⁺ UVD volume emission rate is identical to the production rate of CO₂⁺
 369 (B²Σ_u⁺) multiplied by the branching ratio 0.5. The limb intensity profile of the CO₂⁺ UVD
 370 volume emission rate, which can be directly compared to the observations by
 371 MAVEN/IUVS, is then calculated by integrating the CO₂⁺ UVD volume emission rate
 372 along the line of sight in the limb geometry.

373

374

375 **3. Instruments**

376 The instruments used to constrain the electron and proton fluxes at the model topside are
 377 the Solar Energetic Particle (SEP) and Solar Wind Electron Analyzer (SWEA) onboard
 378 MAVEN.

379

380 The SEP instrument consists of two sensors: SEP1 and SEP2. Each sensor consists of a
381 pair of double-ended solid-state telescopes to measure 20-1000 keV electrons and 20-
382 6000 keV ions in four orthogonal directions with a field of view of $42^\circ \times 31^\circ$ (Larson et
383 al., 2015). The directions are labeled '1F', '1R', '2F' and '2R', where '1' and '2' denote
384 the SEP instrument sensors (SEP1 and SEP2, respectively), and 'F' and 'R' denote the
385 'forward' FOV and 'reverse' FOV, respectively (Larson et al., 2015). The SEP instrument
386 data used in this study correspond to Level 2 data provided by the Planetary Data System
387 (PDS) (Larson et al., MAVEN SEP Calibrated Data Product Bundle, [https://pds-
388 ppi.igpp.ucla.edu/search/view/?f=yes&id=pds://PPI/maven.sep.calibrated/data/spec](https://pds-ppi.igpp.ucla.edu/search/view/?f=yes&id=pds://PPI/maven.sep.calibrated/data/spec)).

389

390 The SWEA instrument is a symmetric, hemispheric electrostatic analyzer designed to
391 measure the energy and angular distributions of solar wind electrons and ionospheric
392 photoelectrons in the Martian environment (Mitchell et al., 2016). The instruments
393 measure electron fluxes in the energy range of 3 eV - 4.6 keV (Mitchell et al., 2016). The
394 SWEA instrument data used in this study correspond to Level 2 data provided by the PDS
395 (Mitchell et al., MAVEN SWEA Calibrated Data Bundle, [https://pds-
396 ppi.igpp.ucla.edu/search/view/?f=yes&id=pds://PPI/maven.swea.calibrated](https://pds-ppi.igpp.ucla.edu/search/view/?f=yes&id=pds://PPI/maven.swea.calibrated)).

397

398 Note that we assume isotropic pitch angle distribution of electrons and protons obtained
399 by SEP and SWEA. For electrons, we used SEP electrons > 30 keV and SWEA < 5 keV,
400 with interpolation between those values. For protons, we used SEP ions > 50 keV because
401 the sensitivity of the SEP ion is low below 50 keV.

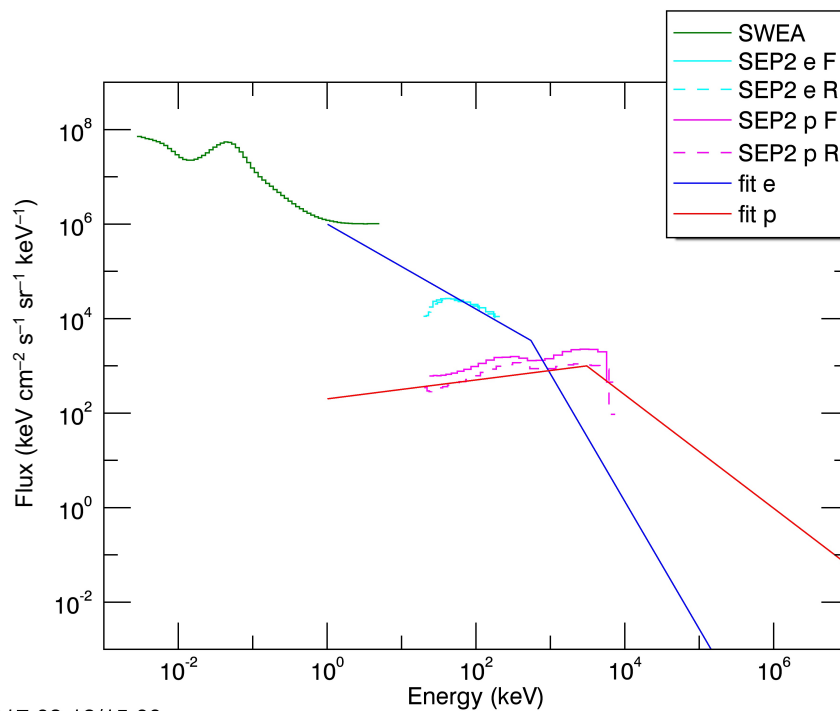
402

403 We used the median value of the electron and proton fluxes obtained by SEP and SWEA
404 instruments of the orbit 437 for the December 2014 SEP event. The orbit 437 was chosen
405 because the observed auroral emission was the brightest (Schneider et al., 2015). The
406 channel of the SEP instrument was selected as 1F; the electron and proton fluxes of the
407 SEP instrument were used only when the SEP instrument attenuator was open. The
408 electron and proton flux spectra for the December 2014 SEP event used in this study are
409 shown in Figure 4 (a).

410

411 So far, the September 2017 SEP event has been the strongest solar energetic particle event
412 detected by the SEP instrument at Mars. The high fluxes of energetic electrons and ions
413 during this event caused the instrument mechanical attenuator to automatically close in
414 order to reduce the detected flux of particles and prevent saturation of the instrument.

415 However, the flux of highest energy particles (above a few MeV) that can penetrate the
 416 instrument housing (and the attenuator) was strong enough to contribute to a significant
 417 portion of the differential energy flux measured by SEP at the range of energies that are
 418 typically associated with particles that can be stopped by the attenuator. The level of
 419 background is less severe for the time periods when the SEP attenuators were open so
 420 that it was possible to apply fitting procedures in order to remove this background present
 421 in the data. We fit a series of theoretical ion and electron spectra to the measurements in
 422 all of the SEP energy channels, including coincidence events that are mainly caused by
 423 penetrating particles. In our fitting, we use a realistic model of the instrument geometric
 424 factor and find the ion and electron spectra that produce the best match with the
 425 measurements. The results are shown in Figure 3. The electron and proton flux spectra
 426 for the September 2017 SEP event used in this study are shown in Figure 4 (b). Note that
 427 since the electron and proton fluxes used for the September 2017 SEP event was taken
 428 from the timing just before the flux peak and auroral emission peak, the resulting modeled
 429 auroral emission intensity should be small compared with the IUVS observation reported
 430 by Schneider et al. (2018). For this event, we do not focus on the absolute auroral
 431 emission intensity but on the relative intensity of electron- and proton- induced emissions
 432 and on the shapes of the auroral emission profiles.
 433

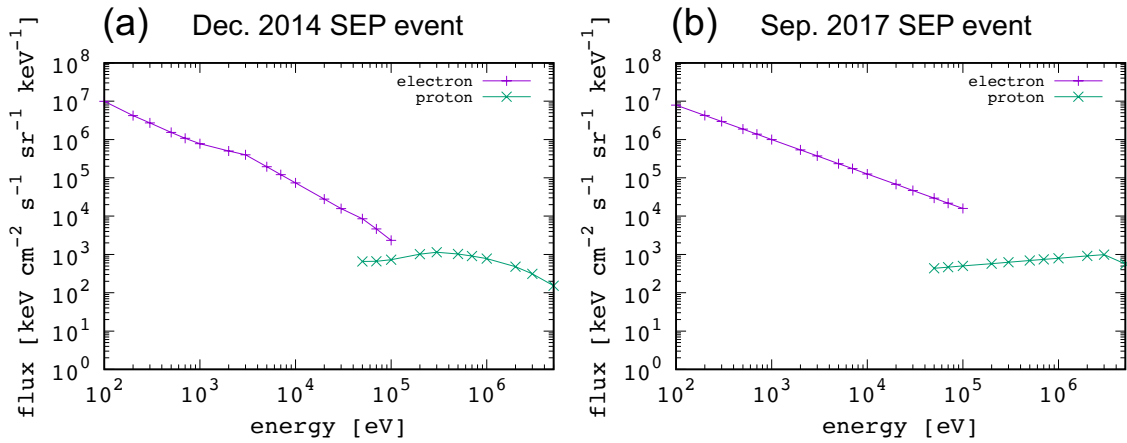


2017-09-12/15:00
 2017-09-12/17:30

434
 435

Figure 3 Electron and proton fluxes measured by SEP and SWEA

436 /MAVEN from 15:00UT to 17:30UT on 12 September 2017. Green line
 437 shows the electron flux observed by SWEA. The cyan solid and dashed
 438 lines show the electron fluxes observed by the SEP2 sensor in the
 439 forward and in the reverse directions, respectively. The violet solid and
 440 dashed lines show the proton fluxes observed by the SEP2 sensor in the
 441 forward and in the reversed directions, respectively. The blue solid line
 442 is the fit used in this paper for the electron fluxes and the red solid line
 443 is that for the proton fluxes.
 444
 445



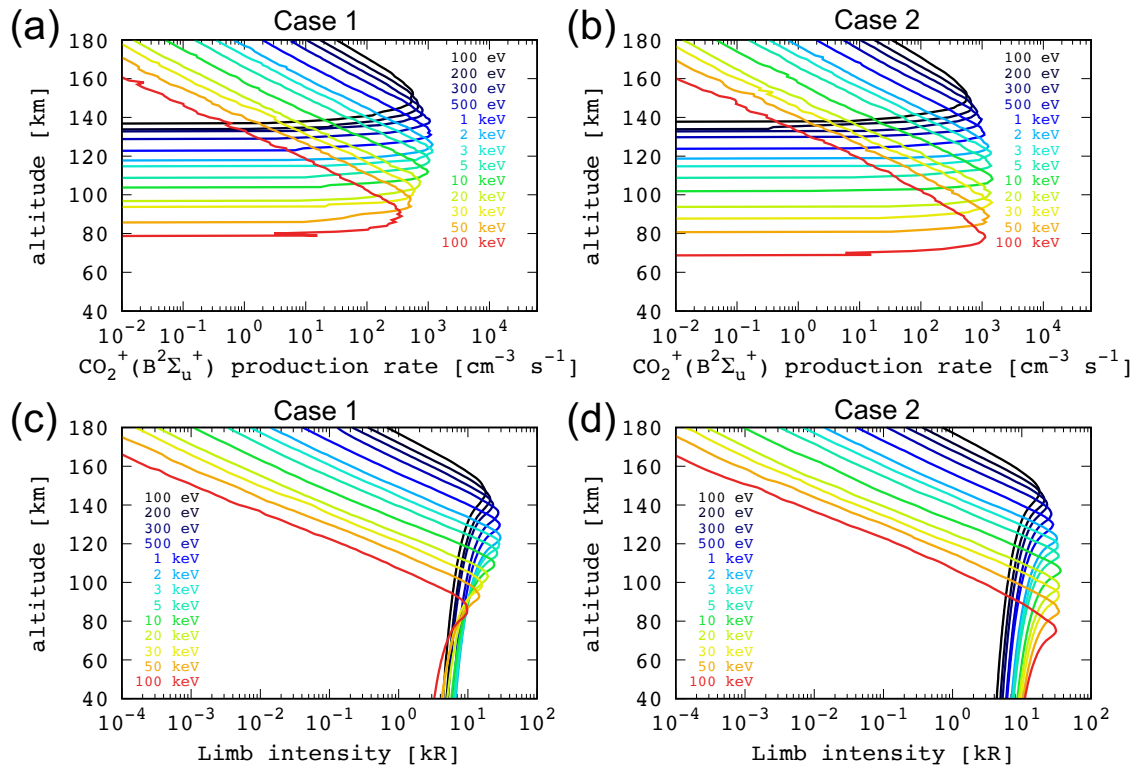
446
 447 Figure 4 (a, b) Electron and proton fluxes for the December 2014 SEP
 448 event and the September 2017 SEP event that were used in this study,
 449 respectively.
 450

451
 452 **4. Results**

453 **4.1 Validation**

454 Since the numerical codes of PTRIP were newly developed, we first compare our model
 455 of electron transport with Gérard et al. (2017). The altitude profile of CO₂ is taken from
 456 Gérard et al. (2017). For simplicity, we ignore other species of the atmosphere in this test
 457 calculation. Our model uses the scattering angle distributions for elastic scattering with
 458 the CO₂ of Porter et al. (1987) for below 500 eV and that of Yalcin et al. (2006) for above
 459 500 eV. Since Gérard et al. (2017) used the value of Porter et al. (1987) even at high
 460 energies, we performed validation calculations for two cases: (1) case 1 used the Porter
 461 et al. (1987) scattering angle distribution at all energies, and (2) case 2 used the Porter et
 462 al. (1987) value for below 500 eV and the Yalcin et al. (2006) value for above 500 eV.

463 The electron flux at the top of the model is 1 mW m^{-2} for all incident energies, which is
464 set to be the same as Gérard et al. (2017). The incident angle is isotropically distributed.
465
466 Figure 5 (a, b) shows the calculated CO_2^+ ($\text{B}^2\Sigma_u^+$) production rate for the two cases, and
467 (c, d) shows the calculated limb intensity of CO_2^+ UVD for the two cases. In case 1, the
468 production rate of CO_2^+ ($\text{B}^2\Sigma_u^+$) and the limb intensity of CO_2^+ UVD are the largest at 2
469 keV and decrease with incident energy above 2 keV. This trend is also visible with the
470 Gérard et al. (2017) value. The peak limb intensity of CO_2^+ UVD in case 1 is 30 kR at 2
471 keV and 10 kR at 100 keV, which is in good agreement with Gérard et al. (2017). In case
472 2, the production rate of CO_2^+ ($\text{B}^2\Sigma_u^+$) and limb intensity of CO_2^+ UVD are almost
473 constant above 500 eV. The production rate of CO_2^+ ($\text{B}^2\Sigma_u^+$) at 100 keV in case 1 is 4
474 times smaller than that in case 2. The penetration altitude of electrons in case 1 is higher
475 than that in case 2. The difference between the two cases comes from the different
476 scattering angle distributions. Figure 6 shows the backscatter probability of electrons at
477 each incident energy for the two cases. In case 1, the backscatter probability increases
478 with incident energy above 500 eV and reaches $\sim 80\%$ at 100 keV. In case 2, the
479 backscatter probability is almost constant at $\sim 30\%$ above 2 keV. In case 1, since the same
480 scattering angle distribution is used above 500 eV, electrons with higher energy have more
481 chances to change of direction because they experience more elastic collisions. In case 2,
482 since scattering becomes more forward-peaked at high energy, the backscatter probability
483 does not increase at high energy. The production rate of CO_2^+ ($\text{B}^2\Sigma_u^+$) and limb intensity
484 of CO_2^+ UVD in case 1 at high energy are smaller than those in case 2 because electrons
485 are more likely to be backscattered before they lose energy via ionization. There remains
486 discrepancy in the penetration altitude of electrons between case 1 and Gérard et al.
487 (2017); the possible reasons are the different total elastic cross section and ionization
488 cross section used in the two models. However, the penetration altitude of electrons
489 during the December 2014 SEP event in our calculation (in case 2) is consistent with
490 Haider and Masoom (2019), as explained in Section 4.2.



491

492

493

494

495

496

497

498

Figure 5 (a, b) Production rate of $\text{CO}_2^+ (\text{B}^2\Sigma_u^+)$ due to electron impacts for each incident electron energy in case 1 and case 2. Case 1 uses the elastic scattering angle distribution of Porter et al. (1987) for all energies, and case 2 uses Porter et al. (1987) below 500 eV and Yalcin et al. (2006) above 500 eV. (c, d) Limb intensity profile of CO_2^+ UVD in case 1 and case 2, respectively. The model topside incident electron flux is 1 mW m^{-2} at each incident energy for the two cases.

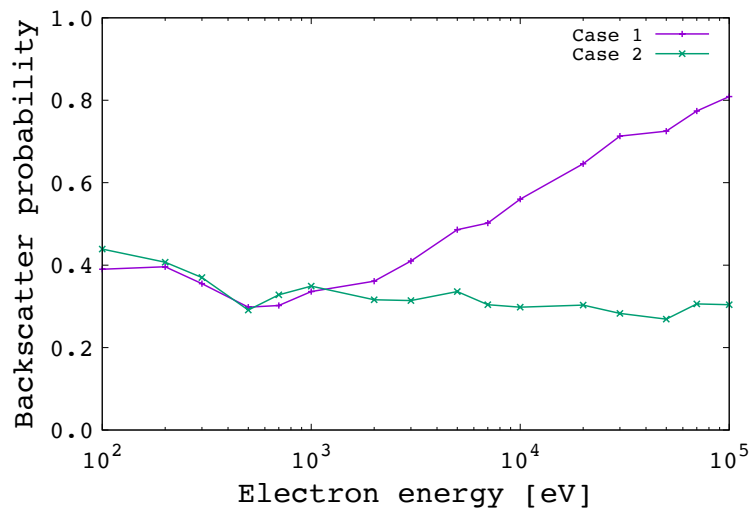
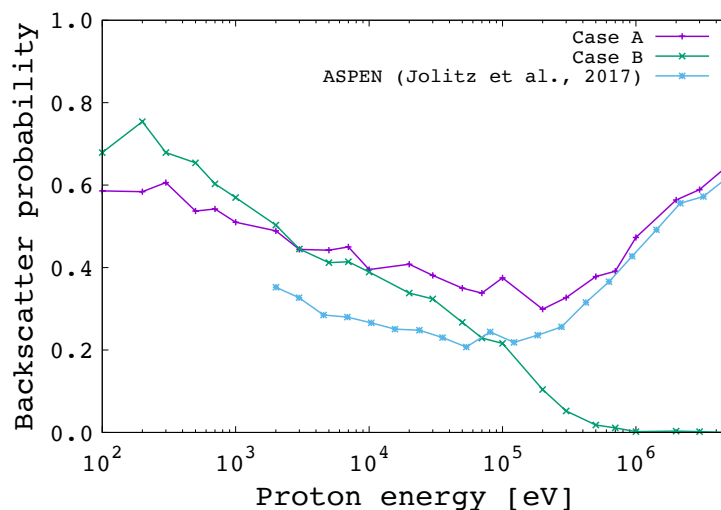


Figure 6 Backscatter probability of different incident electron energies in case 1 and case 2.

Our model of proton and hydrogen atom transport is also compared with previous models. Several models have been proposed for proton and hydrogen atom transport in the Martian atmosphere: a model of fast neutral hydrogen atoms (hereafter called KB01) (Kallio and Barabash, 2001), the Stopping and Range of Ions in Matter model (hereafter called SRIM) (Leblanc et al., 2002), and the Atmospheric Scattering of Protons and Energetic Neutrals (hereafter called ASPEN) (Jolitz et al., 2017). KB01, SRIM and ASPEN were previously compared in Leblanc et al. (2002) and Jolitz et al. (2017) using the test calculation of incident 800 eV neutral hydrogen atoms. One thousand hydrogen atoms of 800 eV were isotropically injected into the Martian atmosphere. Our model predicts that 27% of the energy is deposited into ionization, which agrees with KB01 (27%) and ASPEN (26%). We found that 26% and 24% of energy is deposited into electron stripping and Lyman- α emission, respectively, which agree with KB01 (26% and 30%, respectively). We found that 19% of the energy was deposited into direct neutral heating via elastic collision, which is in close agreement with KB01 (14%), SRIM (16%) and ASPEN (13%). Our model found that 57% of hydrogen atoms were backscattered, which agrees with KB01 (58%) and is larger than ASPEN (32%) and SRIM (10%).

For proton transport, our model uses the differential and the total elastic cross sections

523 described in equations (2) and (4), while ASPEN used the differential and the total elastic
 524 cross sections from KB01, and it predicted that the backscatter probability of protons
 525 increases with incident energy above 100 keV, reaching more than 60% at 5 MeV. Since
 526 they used the scattering angle distribution from KB01 that does not depend on the proton
 527 energy, higher energy protons experience so many elastic collisions that they are more
 528 likely to change of direction. We tested the proton backscatter probability for two cases:
 529 case A used the same differential and total elastic cross section of protons and hydrogen
 530 atoms as KB01, and case B used the differential and total elastic cross section of protons
 531 described in equations (2) and (4) and those of hydrogen atoms from KB01. The
 532 backscatter probabilities of different incident proton energies in the two cases are shown
 533 in Figure 7. In case A, the backscatter probability of protons increases with incident
 534 proton energy above 200 keV and reaches more than 60% at 5 MeV, which is in close
 535 agreement with ASPEN. In case B, the backscatter probability is close to that in case A
 536 below 100 keV, but it decreases with incident proton energy and reaches nearly 0% at 5
 537 MeV because the scattering becomes more likely to be forward-peaked at higher energy.
 538 As described in Section 2.2, since KB01 overestimated the differential elastic cross
 539 section of MeV protons by a few orders of magnitude at large scattering angles, case A
 540 significantly overestimated the backscatter probability, which leads to the
 541 underestimation of the ionization rate at low altitudes where MeV protons deposit energy
 542 into the atmosphere.



543
 544 Figure 7 Backscatter probability of different incident proton energies in
 545 case A and case B. Case A uses the differential cross section, and the total
 546 elastic cross section from KB01 and case B uses the screened Rutherford

547 elastic cross section.

548

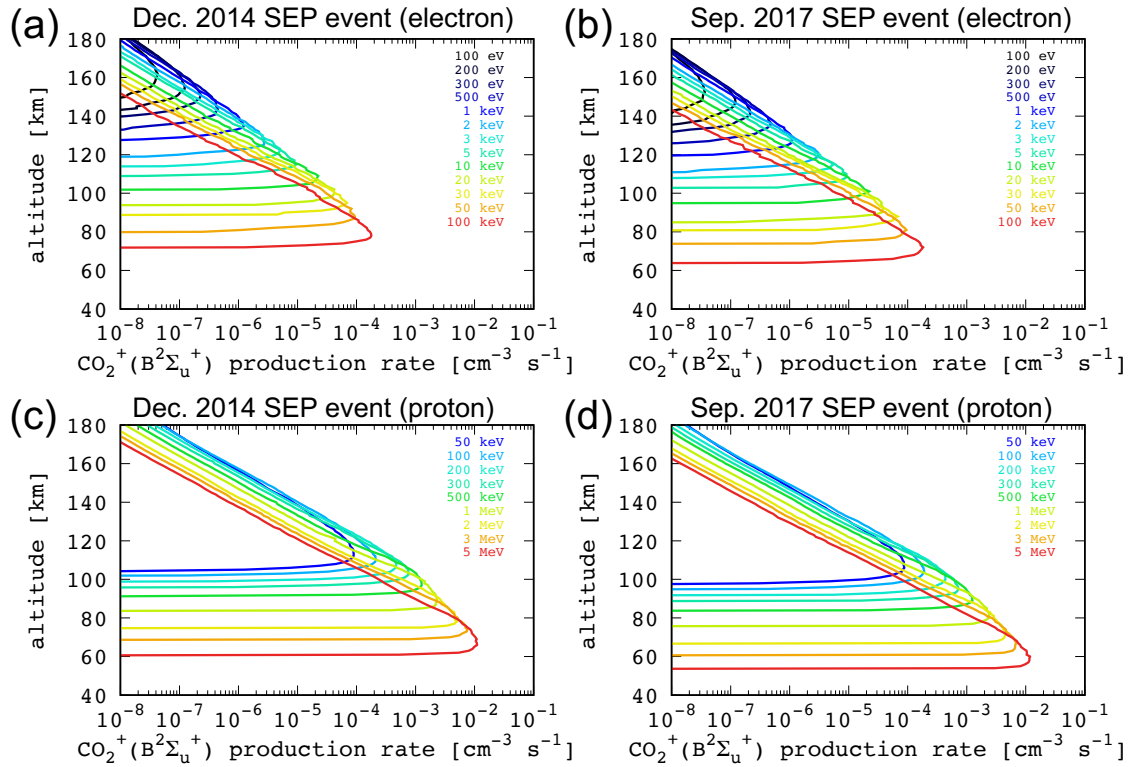
549

550 **4.2 Production Rate of CO_2^+ ($\text{B}^2\Sigma_u^+$) During SEP Events**

551 Figure 8 represents the calculated production rate of CO_2^+ ($\text{B}^2\Sigma_u^+$) with an incident flux
552 of $1 \text{ cm}^{-2} \text{ s}^{-1}$ at each incident energy of electrons and protons at the top of the model on
553 20 December 2014 and on 13 September 2017. The penetration altitude of electrons in
554 our calculation was compared with Haider and Masoom (2019). They calculated the
555 ionization rate during the December 2014 SEP event and found that the ionization rate by
556 100 keV electrons peaks at an altitude of 75 km. The peak altitude of the ionization rate
557 by 100 keV electrons is 75 km in our model, which is precisely consistent with Haider
558 and Masoom (2019). For protons, the penetration altitude of 5 MeV protons is
559 approximately 55-65 km, which is approximately 10-20 km higher than Jolitz et al. (2017).
560 The possible reasons for the discrepancy between our model and Jolitz et al. (2017) are
561 the different atmospheric density profiles, which are not described in Jolitz et al. (2017).
562 Different scattering angle distributions in the elastic collision can also explain this
563 discrepancy with Jolitz et al. (2017) because the smaller differential elastic cross section
564 at a large scattering angle used in PTRIP implies a smaller deviation of the protons when
565 traveling radially and therefore a deeper penetration.

566

567 The penetration altitude at each incident energy is approximately 10 km lower for the
568 September 2017 SEP event than for the December 2014 SEP event. The Ls was 255°
569 (near perihelion) on 20 December 2014 and 60° (near aphelion) on 13 September 2017,
570 corresponding to the season of atmospheric inflation and contraction on Mars,
571 respectively (e.g., Forget et al., 2009).



572

573

574

575

576

577

578

579

580

581

Figure 8 (a, b) Production rate of $\text{CO}_2^+(\text{B}^2\Sigma_u^+)$ with an incident flux of $1 \text{ cm}^{-2} \text{ s}^{-1}$ for each incident energy of electrons at the top of the model during the December 2014 SEP event and September 2017 event, respectively, and (c, d) those of protons during the December 2014 SEP event and September 2017 SEP event, respectively. Note that not all incident energies in the model are shown here to make the figure easier to read.

582

583

584

585

586

587

588

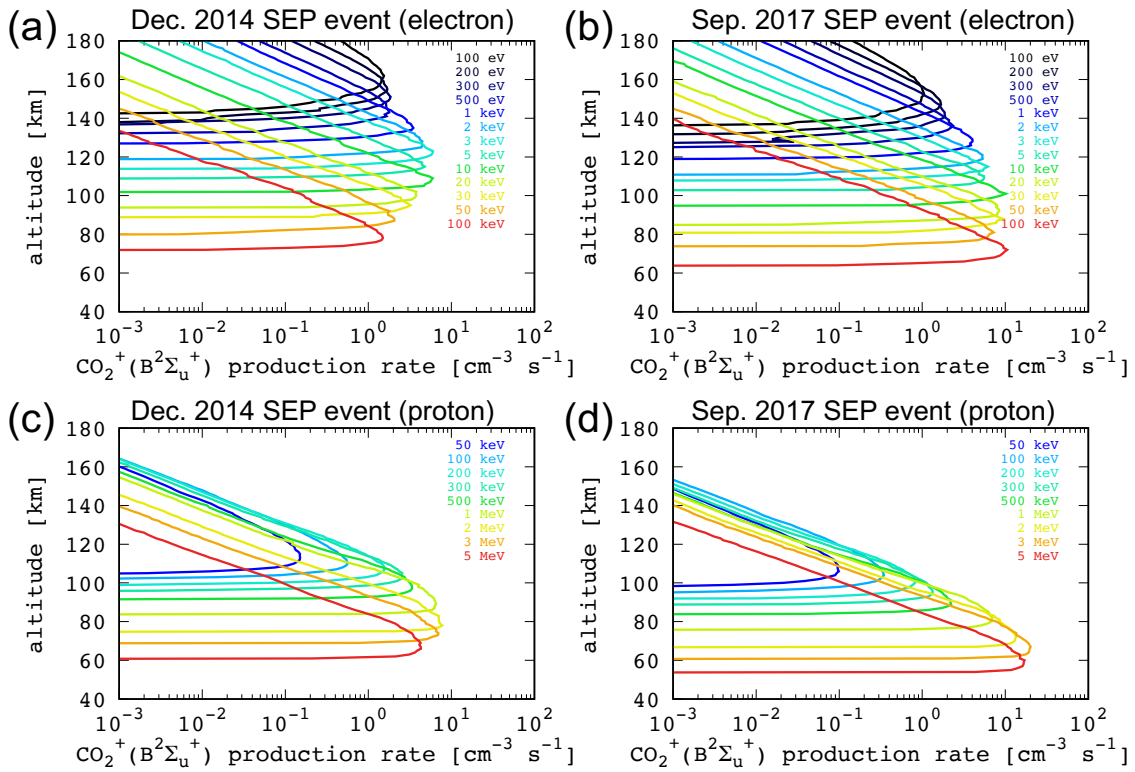
589

590

591

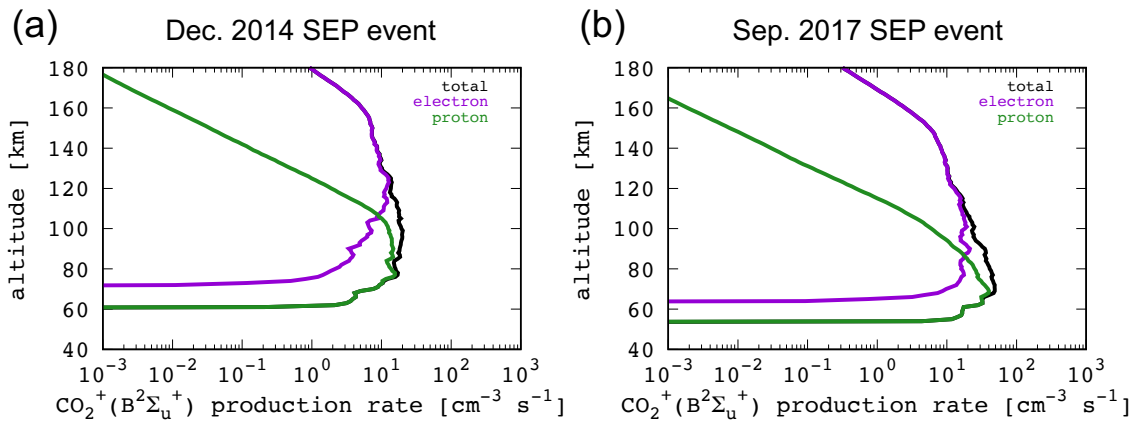
Figure 9 shows the calculated production rate of $\text{CO}_2^+(\text{B}^2\Sigma_u^+)$ for each incident energy of electrons and protons during the December 2014 SEP event and September 2017 SEP event according to equation (5) by using the production rate with an incident flux of $1 \text{ cm}^{-2} \text{ s}^{-1}$ at each incident energy (Figure 8) and electron and proton fluxes observed by MAVEN (Figure 4). A comparison of the total production rate of $\text{CO}_2^+(\text{B}^2\Sigma_u^+)$ between incident electrons and protons during these two SEP events is shown in Figure 10. During the SEP event in December 2014, the largest contribution to the production rate of $\text{CO}_2^+(\text{B}^2\Sigma_u^+)$ due to electron impact occurs at an altitude of approximately 110 km, corresponding to the incident 3-10 keV electrons (Figure 9a). The largest contribution to the production rate of $\text{CO}_2^+(\text{B}^2\Sigma_u^+)$ due to proton and hydrogen atom impacts occurs at

592 80 km altitude by incident 2 MeV protons (Figure 9c). The production rates of CO_2^+
593 ($\text{B}^2\Sigma_u^+$) by electrons and protons both have a peak value of $10 \text{ cm}^{-3} \text{ s}^{-1}$ during this SEP
594 event. During the SEP event in September 2017, the largest contribution to the production
595 rate of CO_2^+ ($\text{B}^2\Sigma_u^+$) due to electron impact occurs at 70 km altitude by incident 100 keV
596 electrons. The largest contribution to the production rate of CO_2^+ ($\text{B}^2\Sigma_u^+$) due to proton
597 and hydrogen atom impacts occurs at 70 km altitude by incident 3 MeV protons. The
598 production rate of CO_2^+ ($\text{B}^2\Sigma_u^+$) by electrons and protons has peak values of $20 \text{ cm}^{-3} \text{ s}^{-1}$
599 and $40 \text{ cm}^{-3} \text{ s}^{-1}$, respectively. For both SEP events, the production rate of CO_2^+ ($\text{B}^2\Sigma_u^+$) is
600 dominated by proton impacts below 100 km altitude and by electron impacts above 100
601 km. It is noted that the limitation of the energy range of PTRIP could affect our simulation
602 of the September 2017 SEP event. The production rate of CO_2^+ ($\text{B}^2\Sigma_u^+$) due to
603 precipitation of both electrons and protons increases with an incident energy up to near
604 the upper limit of the energy range of the calculation. A higher energy than considered in
605 our model would increase the CO_2^+ ($\text{B}^2\Sigma_u^+$) production rate at lower altitudes, which
606 could result in a lower peak altitude and a larger peak production rate than that shown in
607 Figure 10. Incident energy of protons are limited above 50 keV due to the observational
608 limitation of the SEP instrument. Protons below 50 keV could contribute to the production
609 of CO_2^+ ($\text{B}^2\Sigma_u^+$) at altitudes above ~ 110 km, but their contribution can simply be
610 speculated to be less than 1/100 of the peak value due to MeV protons according to Figure
611 9.



612
613
614
615
616
617
618
619
620

Figure 9 (a, b) Production rate of $\text{CO}_2^+ (\text{B}^2\Sigma_u^+)$ due to precipitation of electrons during the December 2014 SEP event and September 2017 event, respectively, and (c, d) those of protons during the December 2014 SEP event and September 2017 SEP event, respectively. These production rates are calculated by using the energy flux observed by MAVEN/SEP and SWEA. Note that not all incident energies in the model are shown here to make the figure easier to read.



621
622

Figure 10 (a, b) Total production rate of $\text{CO}_2^+ (\text{B}^2\Sigma_u^+)$ (black) and the

623 contribution of impacting electrons (purple) and protons (green) during
624 the December 2014 SEP event and September 2017 SEP event,
625 respectively.

626

627

628 **4.3 CO₂⁺ UVD Limb Intensity Profiles During SEP Events**

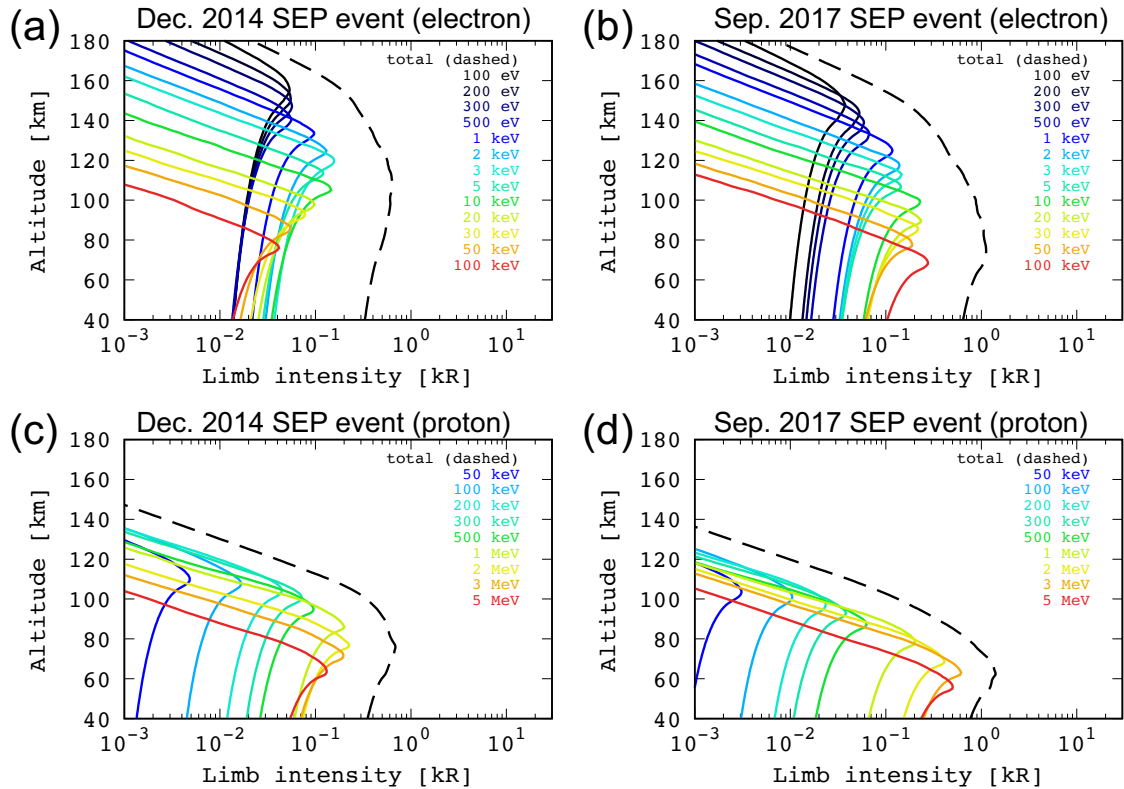
629 The limb intensity profile of CO₂⁺ UVD emissions is calculated by integrating the volume
630 emission rate of CO₂⁺ UVD along the line of sight in the limb geometry. As mentioned in
631 Section 2.5, the volume emission rate of CO₂⁺ UVD is estimated by multiplying the
632 production rate of CO₂⁺ (B²Σ_u⁺) by 0.5. Figure 11 shows the limb intensity profile of CO₂⁺
633 UVD for each incident energy of electrons and protons during the December 2014 SEP
634 event and September 2017 SEP event.

635

636 During the SEP event in December 2014, electron-induced CO₂⁺ UVD emissions are
637 largest at approximately 110 km with an intensity of 1 kR, produced essentially by 3-10
638 keV electrons. As suggested by previous models of diffuse aurora during the December
639 2014 SEP event (Schneider et al., 2015; Gérard et al., 2017; Haider and Masoom, 2019),
640 100 keV electrons reasonably produce CO₂⁺ UVD emissions at low altitudes (70-80 km),
641 as observed by MAVEN; however, the total electron-induced emissions do not peak at
642 low altitudes because low-energy electrons produce brighter emissions at higher altitudes.
643 While electron-induced CO₂⁺ UVD emission peaks at a high altitude of ~110 km, proton-
644 induced CO₂⁺ UVD emission peaks at a low altitude of ~80 km with an intensity of 1 kR
645 due to 1 MeV protons.

646

647 During the September 2017 SEP event, electron-induced CO₂⁺ UVD emissions are largest
648 at approximately 70 km with an intensity of 1 kR due to 100 keV electrons. Proton-
649 induced CO₂⁺ UVD emission peaks at low altitudes of ~65 km with an intensity of 2 kR
650 due to 3 MeV protons. For both SEP events, the electron-induced CO₂⁺ UVD emission
651 profile covers an altitude range between 60 and 140 km, while the proton-induced CO₂⁺
652 UVD emission profile has a narrower altitude range (between 60 and 100 km) owing to
653 the difference in the electron and proton spectral shape as shown in Figure 4.



654

655

656

657

658

659

660

661

662

Figure 11 (a, b) Limb intensity of CO_2^+ UVD due to precipitation of electrons for differential incident energies during the December 2014 SEP event and September 2017 SEP event, respectively, and (c, d) those of protons during the December 2014 SEP event and September 2017 SEP event, respectively. Note that not all incident energies in the model are shown here to make the figure easier to read.

663

664

665

666

667

668

669

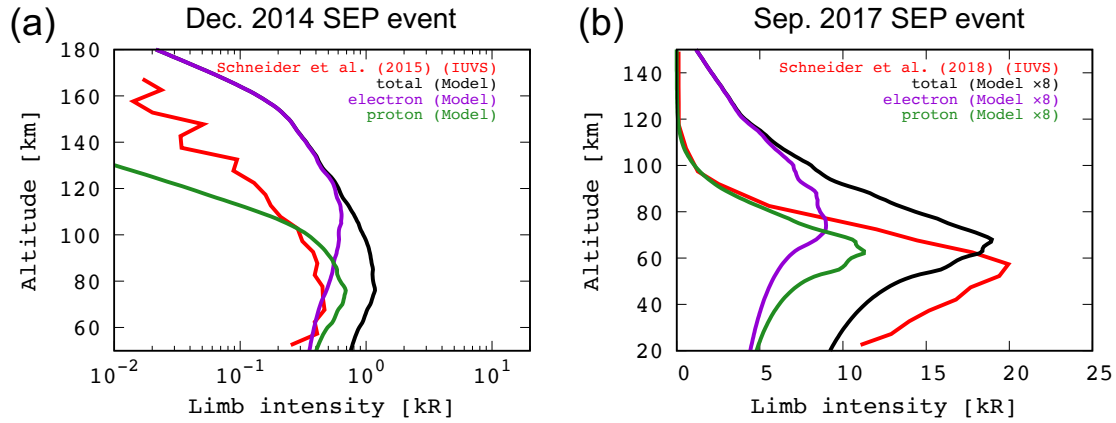
670

671

672

We compared our model results with the observations of CO_2^+ UVD limb intensity obtained by Schneider et al. (2015) and Schneider et al. (2018) for the December 2014 SEP event and September 2017 SEP event, respectively. Figure 12 (a) shows the calculated limb intensity profile of CO_2^+ UVD emissions and the observed profiles during the SEP event in December 2014. The calculated total CO_2^+ UVD limb intensity is 2 times larger than the observation. Our calculated altitude profile peaks at 76 km, which is very close to the observed peak at ~ 70 km. Figure 12 (b) shows the calculated limb intensity profile of CO_2^+ UVD emissions and the observed profiles during the SEP event in September 2017. Since we used the electron and proton flux at the time before the flux peak and auroral emission peak, the calculated limb profiles were multiplied by a factor

673 of 8 to match the observed emission intensity. Our calculated altitude profile peaks at 68
 674 km, which is 10 km higher than the observation.
 675



676

677 Figure 12 (a, b) Total limb intensity of CO_2^+ UVD (black) and
 678 contribution of impacting electrons (purple) and protons (green) during
 679 the December 2014 SEP event and September 2017 SEP event,
 680 respectively. Observed profiles are taken from Schneider et al. (2015)
 681 and Schneider et al. (2018) in the December 2014 SEP event and
 682 September 2017 SEP event, respectively. Note that the calculated limb
 683 profiles for the September 2017 SEP event were multiplied by a factor
 684 of 8 to match the observed emission intensity.

685

686 5. Discussion

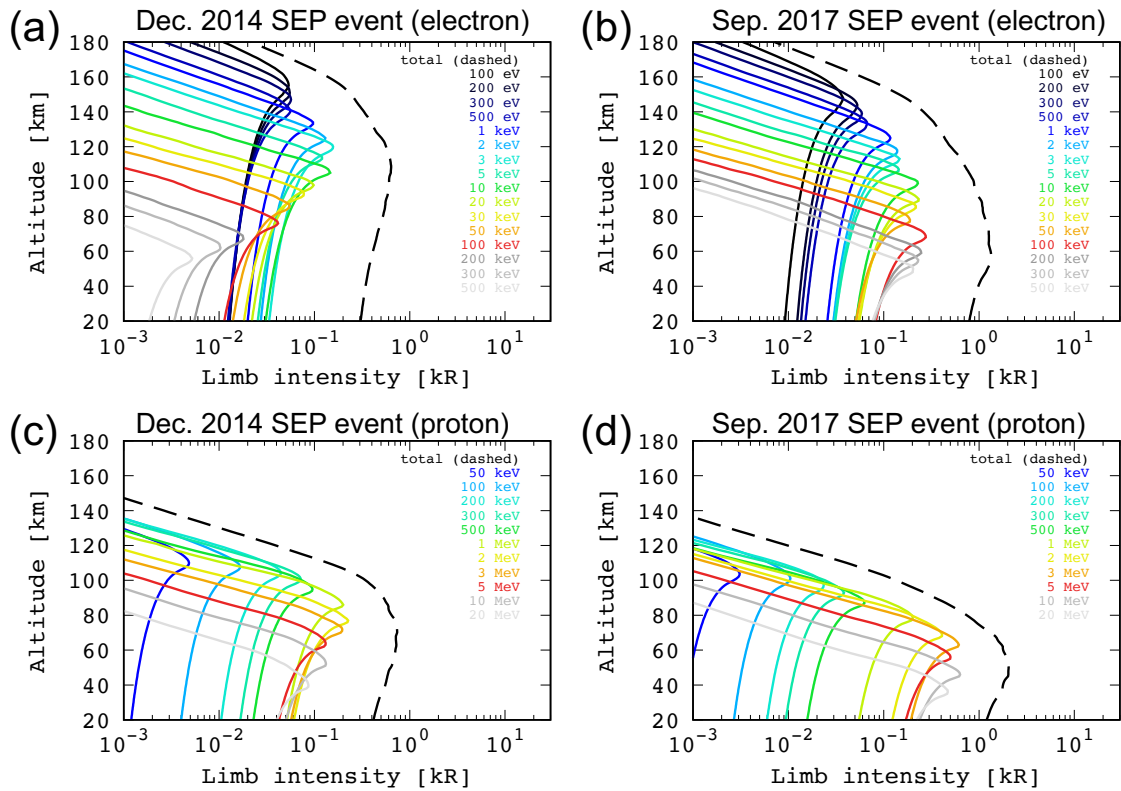
687 Even if we found a good agreement between observations and simulations (Figure 12),
 688 there are several limits when comparing modeled with observed profiles. The results
 689 displayed in Figure 12 depend first on the cross sections and ionizing branching ratio of
 690 the H- CO_2 collision. Since we assumed that most of the cross sections for H- CO_2 used
 691 are identical to the cross sections for H- O_2 collisions, our calculations might be impacted
 692 by this assumption. Another aspect that may have affected our calculations is that we
 693 assumed the branching ratio of CO_2^+ ($\text{B}^2\Sigma_u^+$) to the total CO_2 ionization due to hydrogen
 694 atom impacts to be 0.1.

695

696 As already mentioned in Section 4.2, the upper limit of the energy range considered in
 697 PTRIP could limit our capability to compare the results of our simulation to the IUVS
 698 observations. Extrapolating the cross sections (see Text S1 in the supplementary
 699 materials) and the electron and proton flux considered in this paper allow us to provide a

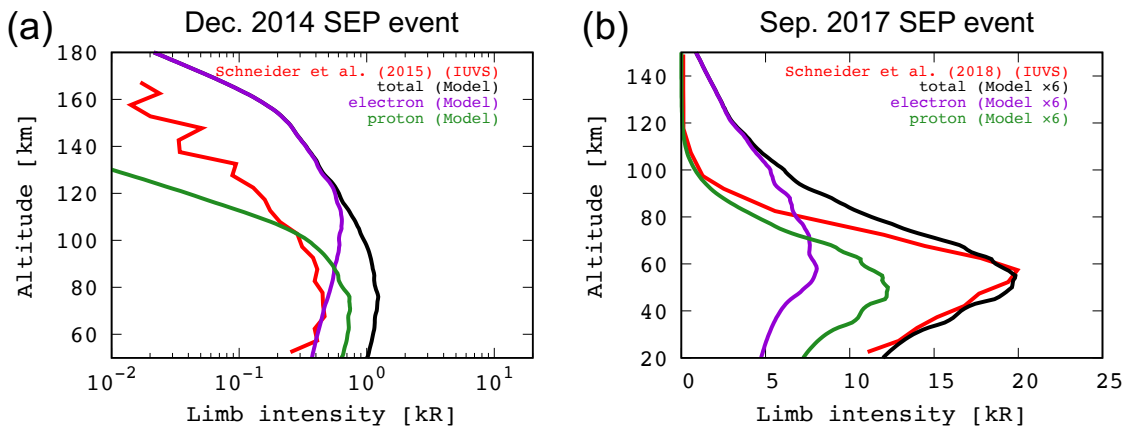
700 first estimate of the potential contributions to the emission due to electrons above 100
701 keV and protons above 5 MeV. For the December 2014 SEP event, since the electron and
702 proton fluxes observed by MAVEN/SEP is limited below 200 keV and 6 MeV,
703 respectively, we simply extrapolated the electron flux above 200 keV and proton flux
704 above 6 MeV logarithmically to estimate the contribution of energetic electrons up to 500
705 keV and energetic protons up to 20 MeV. For the September 2017 SEP event, fitting
706 results of the electron and proton fluxes shown in Figure 3 was used to estimate the
707 contribution of energetic electrons up to 500 keV and energetic protons up to 20 MeV.
708 Figure 13 shows the limb intensity profile of CO_2^+ UVD for each incident energy of
709 electrons up to 500 keV and protons up to 20 MeV during the December 2014 SEP event
710 and September 2017 SEP event. During the December 2014 SEP event, contribution of
711 electrons above 100 keV is comparatively small, while the contribution of protons above
712 5 MeV is comparable to the peak value. During the September 2017 SEP event,
713 contribution of both electrons above 500 keV and protons above 5 MeV are comparable
714 to the peak value. A comparison between our model results with energy extension and the
715 IUVS observations is shown in Figure 14. Note that the calculated limb profiles for the
716 September 2017 SEP event were multiplied by a factor of 6 to match the observed
717 emission intensity. During the December 2014 SEP event, the shapes, the peak altitude
718 and the intensity of CO_2^+ UVD limb profiles does not largely change even if we take into
719 account the contribution of more energetic electrons and protons. During the September
720 2017 SEP event, the calculated limb intensity profile changed below 70 km altitude and
721 it peaks at 55 km, which is in good agreement with the IUVS observation.

722



723
 724
 725
 726
 727
 728
 729
 730
 731
 732

Figure 13 (a, b) Limb intensity of CO_2^+ UVD due to precipitation of electrons for differential incident energies during the December 2014 SEP event and September 2017 SEP event, respectively, and (c, d) those of protons during the December 2014 SEP event and September 2017 SEP event, respectively. Electron and proton energy ranges are extended to 500 keV and 20 MeV, respectively. Note that not all incident energies in the model are shown here to make the figure easier to read.



733

734 Figure 14 (a, b) The contribution of impacting electrons up to 500 keV
735 (purple) and protons up to 20 MeV (green) to the CO₂⁺ UVD limb
736 intensity, and the total limb intensity of CO₂⁺ UVD (black) during the
737 December 2014 SEP event and September 2017 SEP event, respectively.
738 Observed profiles are taken from Schneider et al. (2015) and Schneider
739 et al. (2018) in the December 2014 SEP event and September 2017 SEP
740 event, respectively. Note that the calculated limb profiles for the
741 September 2017 SEP event were multiplied by a factor of 6 to match the
742 observed emission intensity.

743
744

745 The penetration altitude of incident particles strongly depends on the neutral atmospheric
746 temperature. The Martian atmosphere is known to exhibit large variability with respect to
747 season, latitude and local time (e.g., Forget et al., 2009). A different atmospheric
748 temperature would impact, as a first order, the altitude profile of the emission brightness.
749 Since we obtained rather good agreement between the simulated altitude profile of the
750 emission brightness and the observed profile for the two SEP events, our choice of
751 atmospheric density profiles for both events were close to the real atmospheric conditions
752 at that time.

753

754 We did not take into account the effects of the magnetic field. Electrons are expected to
755 be guided to the regions of open magnetic field lines, and they are unlikely to penetrate
756 into close field line regions (Lillis et al., 2011; Jolitz et al., 2021). Proton penetration to
757 low altitudes is also expected to be depleted in regions of strong crustal fields (Leblanc
758 et al., 2002). Due to the different gyro radii of electrons and protons, different sensitivities
759 to the magnetic field strength and configuration are expected (Bisikalo et al., 2017).

760

761 We provide possible explanations for the overestimation of the modeled CO₂⁺ UVD limb
762 intensity compared to the IUVS observations. Since the SEP-induced CO₂⁺ UVD
763 emission peaks at low altitudes, CO₂⁺ UVD could have been absorbed by the Martian
764 atmosphere if there is an absorber of CO₂⁺ UVD. Ozone has a strong absorption line
765 around the wavelength of CO₂⁺ UVD ~289 nm. The absorption cross section of ozone at
766 289 nm is about 10⁻²² m² (Gröller et al., 2018) and the maximum density of ozone is 10¹⁵
767 m⁻³ above an altitude of 50 km (Lebonnois et al., 2006). Integrating the optical depth
768 along the line of sight over a distance of 1000 km using the above cross section and
769 density of ozone yields an upper limit of the optical depth of 0.1 at 289 nm, which is

770 insufficient to absorb CO_2^+ UVD emission by the Martian atmosphere above an altitude
771 of 50 km.

772

773 SEP shadowing by Mars could reduce the SEP ion flux on the nightside of Mars. The
774 Martian Radiation Environment Experiment (MARIE) measurements onboard Mars
775 Odyssey found that the count rate of SEP ions (20-200 MeV) near Mars showed
776 modulation during solar events in October 2002 (Luhmann et al., 2007). They showed
777 that the modulation of the SEP ion flux near Mars resulted from the shadowing of the
778 SEP ion flux and the orientation of the interplanetary magnetic field (IMF). Lillis et al.
779 (2016) reported the anisotropy of SEP ions near Mars, which was suggested to be caused
780 by shadowing by Mars and the configuration of the magnetic field. Since the location and
781 the timing of the observation of electron and proton fluxes made by MAVEN/SEP and
782 SWEA were not precisely the same as the observations of the auroral emission made by
783 MAVEN/IUVS, SEP shadowing might have reduced fluxes at the origin of IUVS
784 observations. Shadowing of the SEP event by Mars might largely explain the factor of 2
785 of the difference between the observed emission brightness and the simulated brightness
786 at the SEP event on 20 December 2014. Another aspect that might reduce the model
787 emission rate is the calculation geometry. Our calculation used the plane-parallel
788 atmosphere, but if we apply a spherical atmosphere, MeV protons with pitch angles larger
789 than 60 degrees at an altitude of 500 km do not penetrate deep into the atmosphere but go
790 through the upper atmosphere and exit the atmosphere because of their gyro radii, which
791 are on the order of the planetary radius. The geometric effect is effective for only protons
792 with energies larger than MeV, so the emission rate due to these protons could be reduced
793 by a factor reaching ~ 2 . For electrons, only a few percent of the SEP electrons can reach
794 the atmosphere due to the magnetic mirror effect (Jolitz et al., 2021), which might be
795 applicable to low-energy protons.

796

797

798 **6. Conclusions**

799 Previous studies were not able to reproduce the observed SEP-induced CO_2^+ UVD auroral
800 emission profiles with precipitating energetic electrons considering the electron energy
801 flux during SEP events observed by MAVEN (Schneider et al., 2015; Gérard et al., 2017;
802 Haider and Masoom, 2019). This study aimed to reproduce the observed CO_2^+ UVD
803 profiles by taking into account the contribution of energetic protons reaching MeV
804 energies. We developed a Monte Carlo model, PTRIP, which solves the transport of
805 electrons, protons and hydrogen atoms through the Martian atmosphere. PTRIP is used

806 to investigate the contribution of electron- and proton-induced CO_2^+ UVD emissions by
807 using the electron and proton fluxes observed by MAVEN. The PTRIP model was
808 validated by comparing our results with previous models (Kallio and Barabash, 2001;
809 Leblanc et al., 2002; Jolitz et al., 2017; Gérard et al., 2017; Haider and Masoom, 2019).
810 Our results showed that proton-induced CO_2^+ UVD emission profiles are brighter,
811 narrower in altitude, and have a lower peak altitude than electron-induced CO_2^+ UVD
812 emission profiles. The sum of the electron- and proton-induced CO_2^+ UVD emission
813 profiles displays similar shapes and altitude peaks as those of the observed profiles
814 (Schneider et al. 2015; Schneider et al. 2018), and extension of energy up to 500 keV for
815 electrons and 20 MeV for protons enabled us to obtain the emission profiles that are more
816 similar to the observations. However, the calculated intensity is larger than the observed
817 intensity by a factor of 2 during the December 2014 SEP event, a discrepancy that might
818 be explained by SEP shadowing (Lillis et al., 2016), calculation geometry effect, and
819 magnetic mirror effect (Jolitz et al., 2021). Therefore, the contribution of energetic
820 protons help to reconcile the in situ observations of the SEP electrons and proton fluxes
821 onboard MAVEN with the observed emission brightness observed by MAVEN/IUVS
822 (Schneider et al., 2015, 2018) during the two SEP events. This conclusion should be
823 confirmed by considering other SEP events and completed by taking into account other
824 possible effects that can impact the reconstructed emission brightness profiles. However,
825 it also invites more accurate investigations of the other possible effects of an SEP event
826 in Mars' atmosphere, such as atmospheric heating or induced low altitude chemistry.

827

828

829 **Acknowledgements**

830 The modeling data supporting the figures presented in this paper are available at
831 <https://doi.org/10.5281/zenodo.5651712>. This work was supported by JSPS KAKENHI
832 Grant Number JP18H05439, JP18KK0093, JP19H00707, 19K03943, JP20H00192, and
833 JP20H04605, and NINS Astrobiology Center satellite research. Y. Nakamura is supported
834 by the International Joint Graduate Program in Earth and Environmental Sciences,
835 Tohoku University (GP-EES). FL acknowledges the support by the ANR HELIOSARES
836 (ANR-09- BLAN-0223), ANR MARMITE-CNRS (ANR-13-BS05-0012-02) and by the
837 “Système Solaire” program of the French Space Agency CNES. Y. Nakamura would like
838 to acknowledge J. Halekas, T. Hara, R. D. Jolitz, X. Shaosui, and N. M. Schneider for
839 their help in processing the particle flux data observed by MAVEN/SEP and SWEA.

840

841

842 **Reference**

- 843 Basu, B., Jasperse, J. R., Robinson, R. M., Vondrak, R. R., and Evans, D. S. (1987). Linear
844 transport theory of auroral proton precipitation: A comparison with observations, *J.*
845 *Geophys. Res.*, 92, 5920-5932, doi:10.1029/JA092iA06p05920.
- 846
- 847 Bertaux, J. L., Leblanc, F., Witasse, O., Quemerais, E., Lilensten, J., Stern, S. A., &
848 Korablev, O. (2005). Discovery of an aurora on Mars, *Nature*, 435, 790-794,
849 doi:10.1038/nature03603.
- 850
- 851 Bhardwaj, A., and Jain, S. K. (2009). Monte Carlo model of electron energy degradation
852 in a CO₂ atmosphere, *J. Geophys. Res.*, 114, A11309, doi:10.1029/2009JA014298.
- 853
- 854 Bhardwaj, A., and Jain, S. K. (2013). CO Cameron band and CO₂⁺ UV doublet emission
855 in the dayglow of Venus: Role of CO in the Cameron band production, *J. Geophys. Res.:*
856 *Space Physics*, 118, 3660-3671, doi:10.1002/jgra.50345.
- 857
- 858 Bisikalo, D. V., Shematovich, V. I., Gérard, J. -C., Hubert, B. (2017). Influence of crustal
859 magnetic field on the Mars aurora electron flux and UV brightness, *Icarus*, 282, 127-135,
860 doi:10.1016/j.icarus.2016.08.035.
- 861
- 862 Brain, D. A., Halekas, J. S., Peticolas, L. M., Lin, R. P., Luhmann, J. G., Mitchell, D. L.,
863 et al. (2006). On the origin of aurorae on Mars, *Geophys. Res. Lett.*, 33, L01201,
864 doi:10.1029/2005GL024782.
- 865
- 866 Deighan, J., Jain, S. K., Chaffin, M. S., Fang, X., Halekas, J. S., Clarke, J. T., et al. (2018).
867 Discovery of proton aurora at Mars, *Nature Astronomy*, 2(10), 802-807,
868 doi:10.1038/s41550-018-0538-5.
- 869
- 870 Ehresmann, B., Hassler, D. M., Zeitlin, C., Guo, J., Wimmer-Schweingruber, R. F.,
871 Matthiä, D., et al. (2018). Energetic particle radiation environment observed by RAD on
872 the surface of Mars during the September 2017 event, *Geophys. Res. Lett.*, 45, 5305-5311,
873 doi:10.1029/2018GL077801.
- 874
- 875 Fang, X., Lummerzheim, D., and Jackman, C. H. (2013). Proton impact ionization and a
876 fast calculation method, *J. Geophys. Res.: Space Physics*, 118, 5369-5378,
877 doi:10.1002/jgra.50484.

878

879 Forget, F., Montmessin, F., Bertaux, J. - L., González - Galindo, F., Lebonnois, S.,
880 Quémerais, E., Reberac, A., Dimarells, E., and López - Valverde, M. A. (2009). Density
881 and temperatures of the upper Martian atmosphere measured by stellar occultations with
882 Mars Express SPICAM, *J. Geophys. Res.*, 114, E01004, doi:10.1029/2008JE003086.

883

884 Fox, J. L., and Dalgarno, A. (1979). Ionization, luminosity, and heating of the upper
885 atmosphere of Mars, *J. Geophys. Res.*, 84, 7315-7333, doi:10.1029/JA084jA12p07315.

886

887 Gérard, J. -C., Soret, L., Shematovich, V. I., Bisikalo, D. V., and Bougher, S. W. (2017).
888 The Mars diffuse aurora: A model of ultraviolet and visible emissions, *Icarus*, 288, 284-
889 294, doi:10.1016/j.icarus.2017.01.037.

890

891 Green, A. E. S., and Sawada, T. (1972). Ionization cross sections and secondary electron
892 distributions, *Journal of Atmospheric and Terrestrial Physics*, 34, 10, 1719-1728,
893 doi:10.1016/0021-9169(72)90031-1.

894

895 Gröller, H., Montmessin, F., Yelle, R. V., Lefèvre, F., Forget, F., Schneider, N. M., et al.
896 (2018). MAVEN/IUVS stellar occultation measurements of Mars atmospheric structure
897 and composition, *J. Geophys. Res.: Planets*, 123, 1449-1483, doi:10.1029/2017JE005466.

898

899 Haider, S. A., Seth, S. P., Kallio, E., and Oyama, K. I. (2002). Solar EUV and electron-
900 proton-hydrogen atom-produced ionosphere on Mars: Comparative studies of particle
901 fluxes and ion production rates due to different processes, *Icarus*, 159(1), 18-30.
902 doi:10.1006/icar.2002.6919.

903

904 Haider, S. A., and Masoom, J. (2019). Modeling of Diffuse Aurora due to Precipitation
905 of H⁺ - H and SEP Electrons in the Nighttime Atmosphere of Mars: Monte Carlo
906 Simulation and MAVEN Observation, *J. Geophys. Res.: Space Physics*, 124, 9566-9576,
907 doi:10.1029/2019JA026688.

908

909 Hassler, D. M., Zeitlin, C., Ehresmann, B., Wimmer-Schweingruber, R. F., Guo, J.,
910 Matthiä, D., et al (2018). Space weather on the surface of Mars: Impact of the September
911 2017 events, *Space Weather*, 16, 1702-1708, doi:10.1029/2018SW001959.

912

913 Hughes, A., Chaffin, M., Mierkiewicz, E., Deighan, J., Jain, S., Schneider, N., et al.

914 (2019). Proton aurora on Mars: A dayside phenomenon pervasive in southern summer, *J.*
915 *Geophys. Res.: Space Physics*, 124, 10533-10548. doi:10.1029/2019JA027140.
916
917 Itikawa, Y. (2002). Cross sections for electron collisions with carbon dioxide, *J. Phys.*
918 *Chem. Ref. Data*, 31, 749, doi:10.1063/1.1481879.
919
920 Itikawa, Y. (2006). Cross sections for electron collisions with nitrogen molecules, *J. Phys.*
921 *Chem. Ref. Data*, 35, 31, doi:10.1063/1.1937426.
922
923 Itikawa, Y. (2009). Cross sections for electron collisions with oxygen molecules, *J. Phys.*
924 *Chem. Ref. Data*, 38, 1, doi:10.1063/1.3025886.
925
926 Itikawa, Y. (2015). Cross sections for electron collisions with carbon monoxide, *J. Phys.*
927 *Chem. Ref. Data*, 44, 013105, doi:10.1063/1.4913926.
928
929 Jackman, C. H., Garvey, R. H., and Green, A. E. S. (1977). Electron impact on
930 atmospheric gases, I. Updated cross sections, *J. Geophys. Res.*, 82(32), 5081-5090,
931 doi:10.1029/JA082i032p05081.
932
933 Jolitz, R. D., Dong, C. F., Lee, C. O., Lillis, R. J., Brain, D. A., Curry, S. M., et al. (2017).
934 A Monte Carlo model of crustal field influences on solar energetic particle precipitation
935 into the Martian atmosphere, *J. Geophys. Res.: Space Physics*, 122, 5653-5669,
936 doi:10.1002/2016JA023781.
937
938 Jolitz, R. D., Dong, C. F., Rahmati, A., Brain, D. A., Lee, C. O., Lillis, R. J., et al. (2021).
939 Test particle model predictions of SEP electron transport and precipitation at Mars, *J.*
940 *Geophys. Res.: Space Physics*, 126, e2021JA029132, doi:10.1029/2021JA029132.
941
942 Kallio, E., and Barabash, S. (2001). Atmospheric effects of precipitating energetic
943 hydrogen atoms on the Martian atmosphere, *J. Geophys. Res.*, 106(A1), 165-177,
944 doi:10.1029/2000JA002003.
945
946 Kozelov, B.V., and Ivanov, V.E. (1992). Monte Carlo calculation of proton-hydrogen
947 atom transport in N₂, *Planetary and Space Science*, 40, 11, 1503-1511, doi:10.1016/0032-
948 0633(92)90047-R.
949

950 Larson, D. E., Lillis, R. J., Lee, C. O., Dunn, P. A., Hatch, K., Robinson, M., et al. (2015).
951 The MAVEN Solar Energetic Particle Investigation, *Space Sci. Rev.*, 195, 153-172,
952 doi:10.1007/s11214-015-0218-z.

953

954 Leblanc, F., Luhmann, J. G., Johnson, R. E., and Chassefiere, E., (2002). Some expected
955 impacts of a solar energetic particle event at Mars, *J. Geophys. Res.*, 107(A5),
956 doi:10.1029/2001JA900178.

957

958 Lebonnois, S., Quémerais, E., Montmessin, F., Lefèvre, F., Perrier, S., Bertaux, J.-L., and
959 Forget, F. (2006), Vertical distribution of ozone on Mars as measured by SPICAM/Mars
960 Express using stellar occultations, *J. Geophys. Res.*, 111, E09S05,
961 doi:10.1029/2005JE002643.

962

963 Lillis, R. J., Fillingim, M. O., and Brain, D. A. (2011). Three-dimensional structure of the
964 Martian nightside ionosphere: Predicted rates of impact ionization from Mars Global
965 Surveyor magnetometer and electron reflectometer measurements of precipitating
966 electrons, *J. Geophys. Res.*, 116, A12317, doi:10.1029/2011JA016982.

967

968 Lillis, R. J., Lee, C. O., Larson, D., Luhmann, J. G., Halekas, J. S., Connerney, J. E. P.,
969 and Jakosky, B. M. (2016). Shadowing and anisotropy of solar energetic ions at Mars
970 measured by MAVEN during the March 2015 solar storm, *J. Geophys. Res.: Space
971 Physics*, 121, 2818-2829, doi:10.1002/2015JA022327.

972

973 Lingam, M., Dong, C., Fang, X., Jakosky, B., and Loeb, A. (2018). The Propitious Role
974 of Solar Energetic Particles in the Origin of Life, *The Astrophysical Journal*, 853:10,
975 doi:10.3847/1538-4357/aa9fef.

976

977 Luhmann, J. G., Zeitlin, C., Turner, R., Brain, D. A., Delory, G., Lyon, J. G., and Boynton,
978 W. (2007). Solar energetic particles in near-Mars space, *J. Geophys. Res.*, 112, E10001,
979 doi:10.1029/2006JE002886.

980

981 Millour, E., Forget, F., Spiga, A., Vals, M., Zakharov, V., Montabone, et al. (2018). The
982 Mars climate database (version 5.3), *From Mars express to ExoMars Scientific Workshop*,
983 Madrid, Spain: ESA-ESAC.

984

985 Mitchell, D. L., Mazelle, C., Sauvaud, J.-A., Thocaven, J.-J., Rouzaud, J., Fedorov, A., et

986 al. (2016). The MAVEN Solar Wind Electron Analyzer, *Space Sci. Rev.*, 200, 495-528,
987 doi:10.1007/s11214-015-0232-1.
988

989 Nigam, B. P. and Sundaresan, M. K. and Wu, T. -Y. (1959). Theory of Multiple Scattering:
990 Second Born Approximation and Corrections to Molière's Work, *Phys. Rev.*, 115, 3, 491-
991 502, doi:10.1103/PhysRev.115.491.
992

993 Noël, S., and Prölss, G. W. (1993). Heating and radiation production by neutralized ring
994 current particles, *J. Geophys. Res.*, 98(A10), 17317-17325, doi:10.1029/93JA01500.
995

996 Porter, H. S., and Jump, F. W. (1978). Analytical total angular elastic electron impact cross
997 sections for planetary atmospheres, *NASA Publ.*, CSC/TM.
998

999 Porter, H. S., Varosi, F., and Mayr, H. G. (1987). Iterative solution of the multistream
1000 electron transport equation: 1. Comparison with laboratory beam injection experiments,
1001 *J. Geophys. Res.*, 92(A6), 5933-5959, doi:10.1029/JA092iA06p05933.
1002

1003 Rieke, Foster F. and Prepejchal, W. (1972). Ionization Cross Sections of Gaseous Atoms
1004 and Molecules for High-Energy Electrons and Positrons, *Phys. Rev. A*, 6, 4, 1507-1519,
1005 doi:10.1103/PhysRevA.6.1507.
1006

1007 Ritter, B., Gérard, J.-C., Hubert, B., Rodriguez, L., and Montmessin, F. (2018).
1008 Observations of the proton aurora on Mars with SPICAM on board Mars Express,
1009 *Geophys. Res. Lett.*, 45, 612–619, doi:10.1002/2017GL076235.
1010

1011 Rudd, M. E., DuBois, R. D., Toburen, L. H., Ratcliffe, C. A., and Goffe, T. V. (1983).
1012 Cross sections for ionization of gases by 5-4000-keV protons and for electron capture by
1013 5-150-keV protons, *Phys. Rev. A*, 28, 6, 3244-3257, doi:10.1103/PhysRevA.28.3244.
1014

1015 Schneider, N. M., Deighan, J. I., Jain, S. K., Stiepen, A., Stewart, A. I. F., Larson, D. et
1016 al. (2015). Discovery of diffuse aurora on Mars, *Science*, 350, 6261,
1017 doi:10.1126/science.aad0313.
1018

1019 Schneider, N. M., Jain, S. K., Deighan, J., Nasr, C. R., Brain, D. A., Larson, D., et al.
1020 (2018). Global aurora on Mars during the September 2017 space weather event, *Geophys.*
1021 *Res. Lett.*, 45, 7391-7398, doi:10.1029/2018GL077772.

1022

1023 Shute, G. G., Robson, D., McKenna, V. R., and Berztiss, A. T. (1962). Elastic scattering
1024 of protons by carbon, *Nuclear Physics*, 37, 535-553, doi:10.1016/0029-5582(62)90289-
1025 4.

1026

1027 Solomon, S. C. (2001). Auroral particle transport using Monte Carlo and hybrid methods,
1028 *J. Geophys. Res.*, 106(A1), 107-116, doi:10.1029/2000JA002011.

1029

1030 Swartz, W. E., Nisbet, J. S., and Green, A. E. S. (1971). Analytic expression for the
1031 energy-transfer rate from photoelectrons to thermal-electrons, *J. Geophys. Res.*, 76(34),
1032 8425-8426, doi:10.1029/JA076i034p08425.

1033

1034 Vahedi, V., and Surrendra, M. (1995). A Monte Carlo collision model for the particle-in-
1035 cell method: applications to argon and oxygen discharges, *Computer Physics*
1036 *Communications*, 87, 1-2, 179-198, doi:10.1016/0010-4655(94)00171-W.

1037

1038 Yalcin, S., Gurler, O., Gultekin, A., and Gundogdu, O. (2006). An analytical expression
1039 for electron elastic scattering cross section from atoms and molecules in 1.0 keV to 1.0
1040 MeV energy range, *Phys. Lett. A*, 356, 2, 138-145, doi:10.1016/j.physleta.2006.04.037.

1041